Acta Materialia 199 (2020) 352–369

Contents lists available at ScienceDirect

Acta Materialia

journal homepage: www.elsevier.com/locate/actamat

Full length article

Effects of lattice distortion and chemical short-range order on the mechanisms of deformation in medium entropy alloy CoCrNi

Wu-Rong Jian[a,1,*], Zhuocheng Xie[b,1], Shuozhi Xu[c], Yanqing Su[a], Xiaohu Yao[b,d,*], Irene J. Beyerlein[a,c,e,2]

[a] Department of Mechanical Engineering, University of California, Santa Barbara, Santa Barbara, California 93106-5070, USA
[b] Department of Engineering Mechanics, South China University of Technology, Guangzhou, Guangdong 510640, P. R. China
[c] California NanoSystems Institute, University of California, Santa Barbara, Santa Barbara, California 93106-6105, USA
[d] State Key Laboratory of Subtropical Building Science, South China University of Technology, Guangzhou, Guangdong 510640, P. R. China
[e] Materials Department, University of California, Santa Barbara, Santa Barbara, California 93106-5050, USA

ARTICLE INFO

Article history:
Received 10 June 2020
Revised 7 August 2020
Accepted 19 August 2020
Available online 24 August 2020

Keywords:
Lattice distortion
Chemical short-range order
Deformation
Medium entropy alloy

ABSTRACT

As the numbers of medium- to high-entropy alloys being studied and impressive structural properties they exhibit increase rapidly, questions regarding the role played by their complex chemical fluctuations rise concomitantly. Here, using a combination of large-scale molecular dynamics (MD), a hybrid MD and Monte-Carlo simulation method, and crystal defect analysis, we investigate the role lattice distortion (LD) and chemical short-range order (CSRO) play in the nucleation and evolution of dislocations and nanotwins with straining in single crystal and nanocrystalline CoCrNi, a medium entropy alloy (MEA). LD and CSRO effects are elucidated by comparisons with responses from a hypothetical pure *A*-atom alloy, which bears the same bulk properties of the nominal MEA but no LD and no CSRO. The analysis reveals that yield strengths are determined by the strain to nucleate Shockley partial dislocations, and LD lowers this strain, while higher degrees of CSRO increase it. We show that while these partials prefer to nucleate in the CoCr clusters, regardless of their size, they find it increasingly difficult to propagate away from these sites as the level of CSRO increases. After yield, nanotwin nucleation occurs via reactions of mobile Shockley partials and is promoted in MEAs, due to the enhanced glide resistance resulting from LD and CSRO.

1. Introduction

As a new class of metallic crystalline materials, multi-principal element alloys (MPEAs), also named medium entropy alloys (MEAs) for ternary systems and high entropy alloys (HEAs) for quaternary, quinary, or senary systems, have been attracting much attention in the structural metals research community [1–7]. These novel alloys are comprised of atoms of, not one main element, but multiple principal elements, distributed in nearly equiatomic proportions at crystalline lattice sites, with typically either a face-centered cubic (FCC) or body-center cubic (BCC) arrangement. In solid solution, their nominal compositions lie in the central region of their multi-component phase diagram [2,7]. In contrast, traditional alloy systems consist of one dominant element, making up the matrix, and several other elements at substantially smaller proportions. Some MPEAs exhibit outstandingly superior mechanical properties than conventional alloys [8–10]. Investigations into the underlying microscopic and nanoscale mechanisms have connected the exceptional MPEA performance with a multiplicity of mechanisms, such as rugged dislocation glide, profuse partial dislocation activity, stacking fault formation, and nanotwinning, and the synergies among them [1,11,12].

Over the past two decades, MPEAs with CoCrNi-based FCC compositions have served as prime examples of the plethora of enhanced structural properties MPEAs can offer. These MPEAs have demonstrated high strength, ductility, fracture toughness, impact and radiation resistance [13]. The two more popular MEAs in this class are the CoCrFeMnNi HEA (also known as the Cantor alloy, the original MPEA) [14] and the CoCrNi MEA [15]. Both alloys possess outstanding fracture toughness at room and cryogenic temperatures [16,17]. Superior to the Cantor alloy, the CoCrNi MEA also achieves high tensile strength, ductility and toughness [18].

* Corresponding author.
E-mail addresses: wurong@ucsb.edu (W.-R. Jian), yaoxh@scut.edu.cn (X. Yao).
[1] Both authors contributed equally to the paper.
[2] Irene Beyerlein was an Editor of the journal during the review period of the article. To avoid a conflict of interest, Professor Beyerlein was blinded to the record and another editor processed this manuscript.

https://doi.org/10.1016/j.actamat.2020.08.044
1359-6454/

Recently, a series of experiments were conducted to investigate the tensile behavior of CoCrNi MEA at cryogenic and room temperatures [19–26]. Again they find that this MEA exhibits a multiplicity of deformation mechanisms, including multiple slip in the early stages of straining, followed by a high propensity for nanotwinning or hierarchical twin network formation. To further tailor the mechanical properties of CoCrNi MEA, some researchers have attempted to introduce nanotwins or dislocations/stacking faults (SFs) by pre-deformation, involving torsion [27–30], cold rolling [31,32], pulsed laser surface treatments [33] and shape-preserving machining [34]. They found that the subgranular twins or SFs influenced defect evolution during subsequent straining and the change resulted in enhancements in the strength and ductility.

The unusual and desirable performance of MEAs have motivated researchers to identify relationships between the active mechanisms and the atomic-scale properties unique to MEAs. Given the mix of neighboring atoms with different atomic sizes, lattice distortion (LD) is one inevitable property within MPEAs. LD varies with the types of atomic species in the MPEA [35–37]. Zhao et al [38,39] built a theoretical model that forecasts a linear correlation between LD and the lattice friction stress in FCC MPEAs and speculated that the LD-induced high friction stress gives MPEAs their high strength. Wang et al [40] found that LD results in varying dislocation dissociation widths along the dislocation line and influences dislocation motion by introducing a relatively higher energy barrier, which leads to its high strength. Yin and Curtin suggested that the excellent strength in the CoCrFeNiPd HEA, compared to the CoCrFeNi HEA, can be mainly attributed to the significant misfit volume of Pd with the other four elements in the mix, i.e., Co, Cr, Fe and Ni [41].

In addition to LD, atomic-scale fluctuations in composition and configuration can also affect the selection of deformation mechanisms. An ideal, statistically uniformly random ensemble of atoms in an MPEA likely exists only at high temperatures. At low temperatures or after long-time annealing, however, a random atomic distribution would decompose into local chemical ordering of certain compositions [42]. If such ordering leads to desirable mechanisms, the range of composition fluctuations can be tailored by choosing the processing or annealing temperature and time schedules. Thus, another critical question arises concerning the influence of short-range chemical ordering on mechanism selection and overall strength and ductility. To this end, the classic concept of chemical short-range order (CSRO) [43–45] has been adopted by MPEA researchers to quantify the deviation from ideal atomic randomness. Direct observation of CSRO in CoCrNi MEA was recently achieved by transmission electron microscopy (TEM) analysis [46]. On the modeling side, however, to date, most atomic-scale simulations, such as molecular dynamics (MD) studies on the plastic behavior of SC and NC MPEAs under tension, compression or shear [47–52] utilize ideally random atomic configurations. Therefore, only the effects of LD and not CSRO were taken into account.

A few recent computational studies have considered CSRO. Ding et al [53] conducted density functional theory (DFT) calculations to study the effect of CSRO in CoCrNi MEA on stacking fault energy (SFE) and obtained a monotonic rise in the SFE, ranging from the negative to the positive values, with increasing degree of CSRO. Also using DFT calculations, Yin et al [54] showed CSRO can reduce the spatial heterogeneity of dislocation core energies and narrow their distribution in a BCC HEA. Li et al [55] utilized atomistic simulations to investigate how CSRO influences dislocation motion in CoCrNi MEA. They found the local CSRO distribution determines the fluctuations in the local energy barrier, requiring segments of a long dislocation to depin from the higher energy barrier locations, thus increasing the strength of the MPEA. Via atomistic simulations in FCC HEA, Antillon et al [56] demonstrated that the critical stress to unpin a dislocation rises with increasing levels of CSRO.

To identify the effects of LD and CSRO separately and to understand their role in changing MPEAs mechanisms or mechanical response, it helps to compare them with a pure metal or traditional alloy that lacks LD or CSRO. Most calculations or experiments to date, however, study dislocation behavior in MPEAs with LD and/or CSRO in an absolute sense. For instance, experimentally, the local atomic structure of the MEA CoCrNi, measured by the extended x-ray absorption fine structure (EXAFS) technique [57], is the average of LD and CSRO over a relatively large volume of material. Some atomistic studies have engaged a single element reference material, to which MPEA computations are compared. For example in [58,59], one or more of the pure metal components of the MPEA have been selected for the reference material. However, such a comparison, while intuitive, may not be straightforward, since pure metals have other physical properties distinct from their parent MPEA alloy, apart from just lack of LD and CSRO. As a possible reference, Varvenne et al. [60] proposed a hypothetical pure metal produced by an average-atom (*A*-atom) interatomic potential [61]. Originating from the embedded-atom-method (EAM) alloy potential, the *A*-atom potential provides a mean-field representation of the MPEA, by approximating the interaction between any two constituent elements as a weighted average. The single atom bond properties are consistent with that of the average MPEA. They showed that it calculates bulk average properties of the random MPEA. Another work [62] demonstrated the similarity in the generalized stacking fault energy (GSFE) curves obtained by the *A*-atom and alloy potentials for two BCC MEAs (MoNbTi and NbTiZr).

In this work, we utilize the MD method to study the effects of LD and CSRO on the deformation mechanisms and tensile behavior of single crystal (SC) and nanocrystalline (NC) CoCrNi MEA. To help reveal their effects in isolation, calculations are repeated on the *A*-atom alloy with no LD or CSRO. To obtain MEAs with different CSRO, hybrid MD and Monte Carlo (MC) simulations are performed using three different annealing temperatures. We consider two SC orientations, one known to produce twins in pure FCC SCs and another not, and two deformation temperatures, 1 K and 300 K, to address thermal effects. In the SCs and NCs of both MEAs and the *A*-atom material, we reveal that yield is controlled by the strain to first nucleate Shockley partials (SPs). It is found here that LD lowers the critical strain to form SPs, while CSRO increases it, causing the *A*-atom SC material to achieve the highest strength and the SC random MEA the lowest. We show that the SPs preferentially nucleate inside the CoCr clusters, but with higher CSRO, find it harder to propagate away from these nucleation site. After yield, both LD and CSRO lead to slower moving SPs, lower densities of mobile SPs, and more nanotwins. Last, in NC MEAs, we demonstrate that both higher densities of mobile SPs and further enhancements in strength can be achieved by introducing subgranular nanotwins prior to mechanical deformation.

2. Methodology

MD calculations are performed using the Large-scale Atomic/Molecular Massively Parallel Simulator (LAMMPS) [63]. The atomic interactions within the MEA Co-Cr-Ni system are represented by the EAM interatomic potential developed by Li et al [55], which has been used in a few recent MD studies involving dislocation nucleation and motion [55,64]. Based on this EAM potential, we develop an *A*-atom potential using the method in Ref. [60], which we then proceed to use here for the *A*-atom material.

To build atomic-scale models for the SC and NC MEAs, we begin with SC and NC models of pure Ni. The dimensions for both models are $\sim$ 27.2 nm $\times$ 27.5 nm $\times$ 27.7 nm. With these dimensions, the SC Ni model has 1.84 million atoms and the NC Ni sample 1.75 million atoms. The SC is oriented with its $[1\bar{1}0]$, $[11\bar{2}]$ and

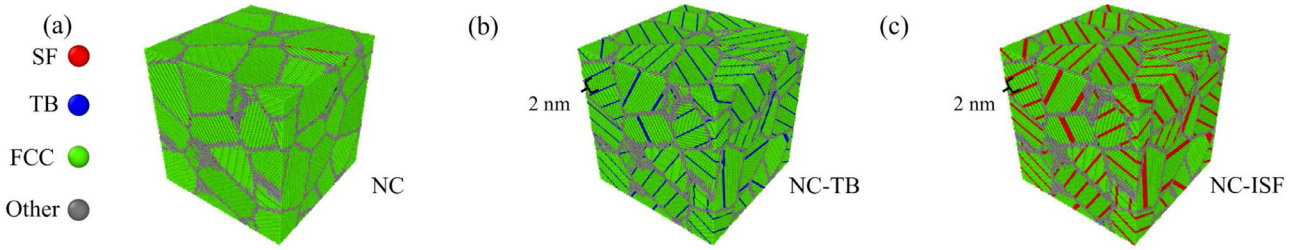

Fig. 1. The atomic configurations of (a) nanocrystals (NC) and those with (b) twin boundaries (TBs) or (c) intrinsic stacking faults (ISFs) inserted. Face-centered cubic (FCC), TB, SF atoms and those with unknown coordination structure are colored by green, blue, red and gray, respectively. The inserted TBs and ISFs are at the same positions of the grains and the spacing between TBs or ISFs is 2 nm. (For interpretation of the references to colour in this figure legend, the reader is referred to the web version of this article.)

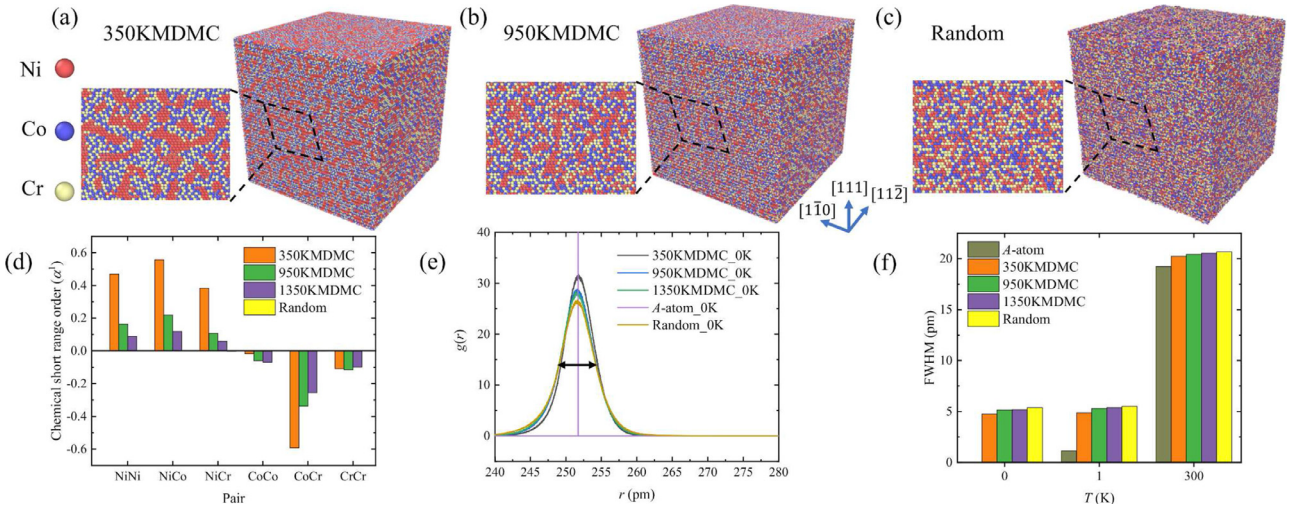

Fig. 2. (a)-(c) The representative atomic configurations for 350KMDMC, 950KMDMC and random single crystalline (SC) CoCrNi samples, respectively. (d) Pairwise chemical short-range order (CSRO) parameter α_{ij}^1 (see methodology) at 0 K, (e) radial distribution function (RDF) $g(r)$ at 0 K and (f) full width at half maximum (FWHM) of $g(r)$ at 0, 1 and 300 K for *A*-atom (see introduction) SC and various SC CoCrNi MEA samples. CSRO parameters for the random sample in (d) and FWHM for 0 K *A*-atom sample in (f) are unrecognizable due to an absolute value that is very close to zero. In (e), FWHM of random sample is shown for example. Here, 350KMDMC, 950KMDMC and 1350KMDMC denote the samples annealed at 350 K, 950 K and 1350 K during hybrid MD/MC simulations, respectively. Random and *A*-atom refer to samples with an ideally uniform random atomic distribution and a mean-field model of the MEA produced by an *A*-atom potential, respectively.

[111] aligned respectively with the *x*-, *y*- and *z*-axes. For the NC Ni model, we use the Poisson-Voronoi tessellation method [65] to generate 27 randomly oriented grains with an average size of ~ 11.4 nm. The resulting nanostructure is shown in Fig. 1(a). For the NC sample, we further investigate the role of pre-existing subgranular nanotwins and intrinsic stacking fault (ISFs) on the deformation response. The twin boundaries (TBs) or ISFs are inserted into every grain with a spacing of 2 nm, following methods described in [66,67]. These nanostructures are built to contain the same density of TBs or ISFs. Fig. 1(b–c) presents the final NC structures containing subgranular nanotwins and ISFs.

Next, the pure Ni SC and NC samples are used to create SC and NC CoCrNi MEAs with completely random atomic distributions. The Ni atoms are randomly substituted by Co or Cr atoms until the desired equal molar composition (Co:Cr:Ni = 1:1:1) is reached. The final result is referred to as the random SC CoCrNi and NC CoCrNi or MEA samples.

Starting with the pure Ni SC and NC samples, three classes of structures of distinctly different CSRO were created with the same nominal chemical composition using a hybrid MD and MC simulation method. First, using the MC technique, the chemical potential differences between Ni and Cr or Co are determined under the semi-grand-canonical (SGC) ensemble at 1500 K. The values obtained from this step are $\Delta\mu_{\mathrm{Ni-Co}} = 0.021$ eV and $\Delta\mu_{\mathrm{Ni-Cr}} = 0.32$ eV. Next, we employ the hybrid MD/MC method under the variance-constrained semi-grand-canonical (VCSGC) ensemble for three different annealing temperatures of 350, 950 and 1350 K. For this step, the MD timestep is set to 2.5 fs [55]. During the MD simulations with the NPT ensemble, the samples are equilibrated at the prescribed annealing temperature. For every 20 MD steps, there is one MC cycle, wherein VCSGC MC operations with $\Delta\mu_{\mathrm{Ni-Co}} = 0.021$ eV, $\Delta\mu_{\mathrm{Ni-Cr}} = 0.32$ eV and a κ parameter of 1000 are performed on a quarter of the atoms, potentially resulting in the replacement of some Ni atoms by Co or Cr atoms. After 60,000 MC cycles, the equilibrium configurations with the equimolar composition and thermodynamically correct occupation of atomic sites are achieved. Last, these structures are then quenched to 1 K and the system energy minimized until all three normal stresses are zero.

Fig. 2 (a–c) displays the atomic configurations for 350KMDMC, 950KMDMC and random SC CoCrNi samples, respectively. We use 'number+K+MDMC' to denote the sample obtained by hybrid MD/MC simulation at a specific annealing temperature. The '350KMDMC', for instance, represents the sample created by using hybrid MD/MC simulation at 350 K. For NC samples, the name 'number+K+MDMC' is followed by 'NC', 'NC-TB' or 'NC-ISF', which represents the NC without TBs or ISFs inserted, the NC with TBs inserted, and NC with ISFs inserted, respectively (Fig. 1(a–c)).

As mentioned in the introduction, a pure metal reference material bearing the same mean properties of the MEA but no SRO or LD, called the *A*-atom material, is constructed and tested alongside the MEAs. To build the SC and NC *A*-atom counterparts, we

use the same methods as those described for Ni but with *A*-atoms instead.

For each structure, the degree of CSRO and LD are quantified. CSRO is measured using Warren-Cowley SRO parameters, $\alpha_{ij}^n = \frac{p_{ij}^n - c_j}{\delta_{ij} - c_j}$, where n means the nth nearest-neighbor shell of the central i-type atom, p_{ij}^n denotes the probability of a j-type atom being around an atom of type i within the nth shell, c_j is the concentration of j-type atom, and δ_{ij} is the Kronecker delta function [44,45]. Accordingly, a value of zero represents a system with completely random atomic distribution. A tendency for segregation or local ordering corresponds to a positive α_{ij}^n for pairs of the same species (i.e., $i = j$) or a negative α_{ij}^n for those of different species (i.e., $i \neq j$), respectively. Larger positive values for same species pairs or larger negative values for unlike species pairs signify higher degrees of CSRO. Average LDs for the sample are quantified based on calculating and comparing the radial distribution functions (RDF) $g(r)$ for the MEAs and *A*-atom sample. The $g(r)$ is defined as the first nearest neighbor shell (i.e., $n = 1$) over the interatomic distance r.

As part of verifying the potentials, we compare the lattice constants, cohesive energies, elastic constants, intrinsic and unstable SFEs of the *A*-atom sample and the random CoCrNi MEA in Table B.1 of the Appendix. As shown, the values between the random CoCrNi and *A*-atom samples are similar. The {111} GSFE curves for different CoCrNi MEA samples are also calculated and shown in Fig. A.1(a) in the Appendix using the method in [68]. Each {111} GSFE curve represents an average of 120 distinct, parallel planes in the SC MEA. For the random sample, the intrinsic SFE is negative, consistent with that reported in previous DFT calculations of CoCrNi [53]. We also mention here some additional GSFE calculations in Fig. A.1(b) in the Appendix for the MEAs annealed at increasing temperatures and concomitantly with decreasing CSRO. Overall, they show that larger value of CSRO leads to higher intrinsic SFEs and unstable SFEs.

The final SC and NC structures are used in subsequent deformation loading and property calculations. In tensile loading, the NPT ensemble and periodic boundary conditions (PBCs) along all directions are maintained, a constant strain rate of 5×10^8 s^{-1} is applied, and the MD timestep is reduced to 1 fs. To alter the LD in the MEAs, we perform SC and NC calculations at two loading temperatures (i.e., 1 and 300 K). In the SC tests, we further consider two loading orientations: $[1\bar{1}0]$ or [111]. The $[1\bar{1}0]$ sample is deformed along the x- and the [111] sample along the z-axis. Theoretically, the [111] orientation in tension is known as a twinning orientation for pure FCC crystals, since the stress state promotes the separation distance between two SPs of an extended dislocation to continually expand under increasing stress [69–73]. The $[1\bar{1}0]$ orientation is not expected to promote twinning, since the stress state continually narrows the SP distance with increasing stress. Finally, in the NC tests, the samples are deformed along the x direction. To achieve a uniaxial stress state in all the tests, a zero normal stress is maintained along the other two directions.

To visualize the crystalline defects before and in each strain step, we use the dislocation analysis (DXA) method [74] implemented in OVITO [75]. Four types of defects will be important in the analyses to come, i.e., stair-rods, Hirth locks, Shockley and perfect dislocations. Stair-rods are associated with the sessile segments of Lomer-Cottrell locks, while the stacking faults (SFs) of Lomer-Cottrell locks are counted separately as part of the SF density. Both stair-rods and Hirth locks are sessile and hence regarded as barriers to dislocation motion [76], whereas SP dislocations and perfect dislocations are glissile and enable plasticity. We also use the crystal analysis method of [77] to distinguish SFs from coherent twin boundaries (TBs) and identify crystalline structures, such as FCC, BCC and hexagonal close-packed (HCP). Last, we monitor the strain (or time) evolution of the densities of nanotwins, TBs and SFs. In the NC samples, to consider only lattice dislocations in the interior of grains, we exclude the grain boundary (GB) atoms when carrying out the DXA analysis.

3. Results and discussion

3.1. Single crystalline MEA

3.1.1. Characterization of LD and CSRO

Fig. 2 (a–c) shows the atomic structures of various SC MEAs. Local CoCr ordering and Ni segregation can be seen in the 350KMDMC and 950KMDMC samples in Fig. 2(a) and (b), respectively. Fig. 2(d) presents the average α_{ij}^1 for the SC CoCrNi MEA samples at 0 K. As expected, the random sample has virtually no CSRO, as indicated by the nearly zero absolute values of all α_{ij}^1 parameters. The other CoCrNi SCs, generated at different annealing temperatures, exhibit evidence of CSRO with large values of both α_{CoCr}^1 and α_{NiNi}^1. The lower the annealing temperature, the larger the value of CSRO α_{ij}^1, with the 350KMCMD sample possessing the greatest degree of CSRO.

Fig. 2 (e) shows the $g(r)$ for the *A*-atom and various SC CoCrNi MEA samples at 0 K. When atomic positions in metals deviate from their ideal, regular lattice sites, the full width at half maximum (FWHM) of $g(r)$ expands. At 0 K, only the LD would contribute to the expansion of the FWHM, with larger LD leading to broader FWHM [78]. In the pure *A*-atom metal, all atoms are positioned at ideal lattice sites, the LD is zero, and the FWHM of $g(r)$ is extremely narrow (Fig. 2(e)). The FWHMs of the SC CoCrNi MEAs, on the other hand, are relatively broader, indicating LD.

For these same SCs, Fig. 2(f) compares the FWHM at 0 K, 1 K and 300 K. At finite temperatures, both LD and thermal vibrations contribute to the FWHM. Even for the *A*-atom sample, the FWHM is non-zero at 1 K and 300 K. However, since there is no LD in the *A*-atom sample at any temperature, its FWHM solely results from thermal vibrations. The LD of the CoCrNi MEA samples at finite temperature can, therefore, be estimated by subtracting the FWHM of the *A*-atom sample from that of the CoCrNi MEA sample at the same temperature. Accordingly, from Fig. 2(f), when the temperature increases from 1 K to 300 K, the FWHM differences decrease, indicating a reduction in LD in the CoCrNi MEA samples. This tendency has also been reported previously [78]. The lattice expands with the rise in temperature, reducing the LD since the distortions become less significant within an expanded lattice.

At any finite temperature, the LDs of CoCrNi samples of differing levels of CSRO increase with decreases in the degree of CSRO, indicating a negative correlation between LD and CSRO. Yet, we observe that the CSRO effect on LD is slight, and overall, the LDs among the three MEAs at a given temperature are nearly the same, a result we will exploit later in the analysis.

Based on the LD and CSRO determined for these structures, we proceed to calculate the deformation responses only for a subset of them, namely, the *A*-atom, 350KMDMC, 950KMDMC and random SC CoCrNi samples and the *A*-atom, 350KMDMC and random CoCrNi NC samples.

3.1.2. Single crystal deformation response

Fig. 3 compares the SC tensile stress-strain response for the three MEAs and the *A*-atom sample when tested in two crystallographic directions and at 1 K and 300 K. The 1 K deformation responses exhibit similar characteristics, displaying a linear rise in stress with strain to a peak value, followed by a steep drop to a lower, non-zero stress. If we assign the strength to this peak stress, then the *A*-atom material provides a substantially higher strength than the MEAs. Among the MEAs, the differences are relatively small, with the random MEA giving the lowest strength for a given test direction and temperature.

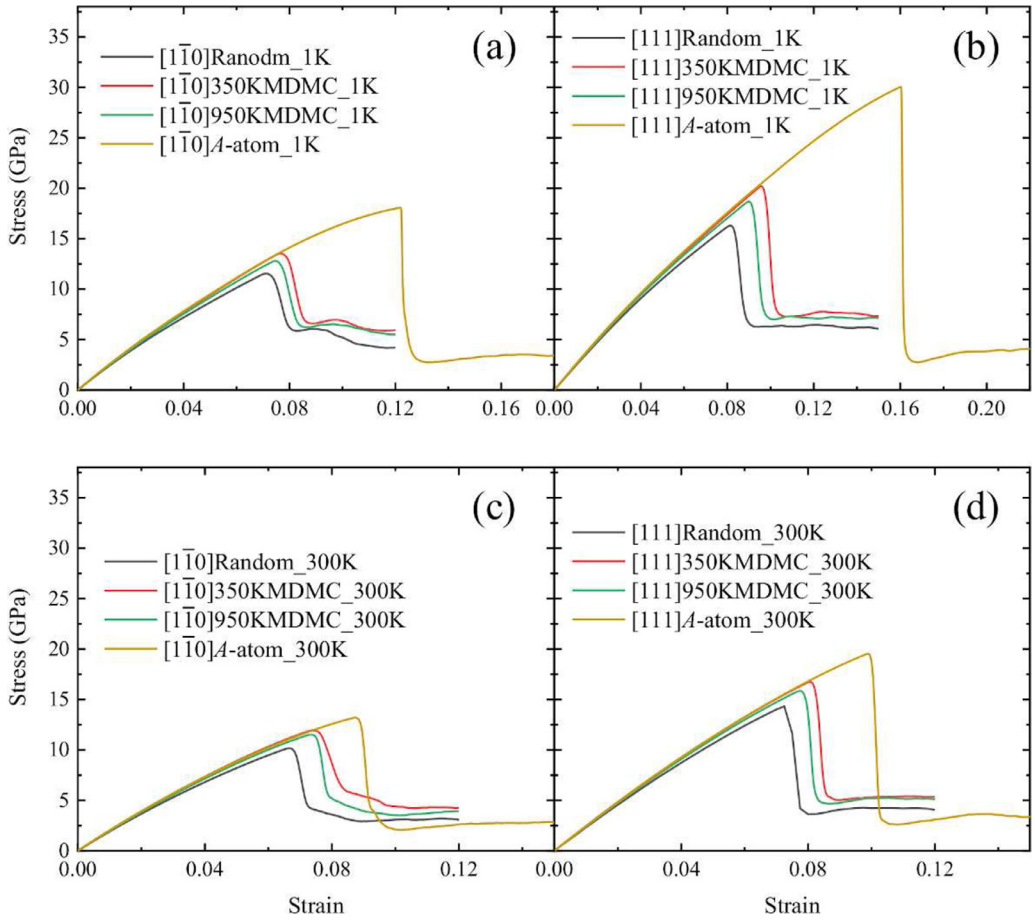

Fig. 3. Tensile stress-strain curves for SC CoCrNi and *A*-atom samples at (a)-(b) 1 K and (c)-(d) 300 K deformed along the [1$\bar{1}$0] and [111] directions, respectively.

When elevating the temperature from 1 K to 300 K, all SCs experience a reduction in the peak stress and strain at which the peak stress is reached. The shape of the stress-strain curves and the rank order among the *A*-atom and MEAs is, however, preserved. While the weakening effect of temperature can be anticipated, it is interesting to note that the *A*-atom experiences the largest drop in strength compared to all MEAs, suggesting an enhanced stability with respect to temperature for the MEA.

In pure metals, the [1$\bar{1}$0] >orientation is expected to be weaker than the [111] orientation, an anisotropy that has been reported in many prior experimental studies [79–83]. As confirmation, the pure metal, *A*-atom sample, exhibits the expected anisotropy in strength with [111] > [1$\bar{1}$0]. The same anisotropy also emerges in all three MEAs at both temperatures. Evidently, the CSRO and LDs existing in the MEAs do not alter the conventional SC anisotropy. In the *A*-atom SCs, however, the anisotropy is more severe than in the MEA SCs. Generally, the lower plastic anisotropy of the MEA SC would be considered desirable and suggest more homogeneous deformation.

The strength of FCC metals has been linked to the unstable SFE γ^{usf} and its association as an energy barrier to emit a leading SP [84]. Fig. A.1(a) compares the GSFE curves for the *A*-atom material and the MEAs, showing only slight differences in their unstable SFE γ^{usf}. Thus, the substantially stronger *A*-atom single crystal over the MEA crystals and the differences in strengths among the MEAs cannot be explained simply by their γ^{usf}. In what follows, we investigate the role played by CSRO and LD, two MEA characteristics not present in the *A*-atom material, in governing their strengths.

3.1.3. Investigating the effects of lattice distortion

To further isolate the effects of LDs from those of CSRO, we analyze the deformation mechanisms underlying the responses of the random CoCrNi and *A*-atom samples. The random CoCrNi bears LDs and the *A*-atom does not, while neither one possesses CSRO. Fig. 4 shows the strain evolution in the density of mobile SPs and perfect dislocations, SFs and TBs, and stored dislocations for the random CoCrNi and *A*-atom at 1 K in the two test directions. The analysis shows that in every SC, the contribution from glide of SPs is large but that from perfect dislocations is minimal. It is also found that the peak stress corresponds to the moment when SPs first nucleate and SFs concomitantly form, indicating that the SCs deform elastically up to the peak stress. The *A*-atom has a much higher Young's modulus and strain to first SP nucleation than the random MEA. These comparisons, thus, associate LD with a reduction in both the Young's modulus and strain to first SP formation.

As straining continues after the peak stress is reached, the stress drops precipitously as SPs continue to proliferate and propagate. Within this post-yield straining period, the deformation mechanisms that ensue depend on test direction. As mentioned, based on pure metal FCC behavior, some twinning is expected to occur in the [111] SC tensile test but not in the [1$\bar{1}$0] SC tensile test. Consistent with conventional FCC SC response, in the *A*-atom [111] SC, a small fraction of nanotwins form and propagate, as seen by the small rise in TB density shortly after SP formation in Fig. 4(h). In the *A*-atom [1$\bar{1}$0] SC, the deformation continues to be accommodated predominantly by SP motion followed by SF formation as seen in Fig. 4(g). More dislocation activities, in-

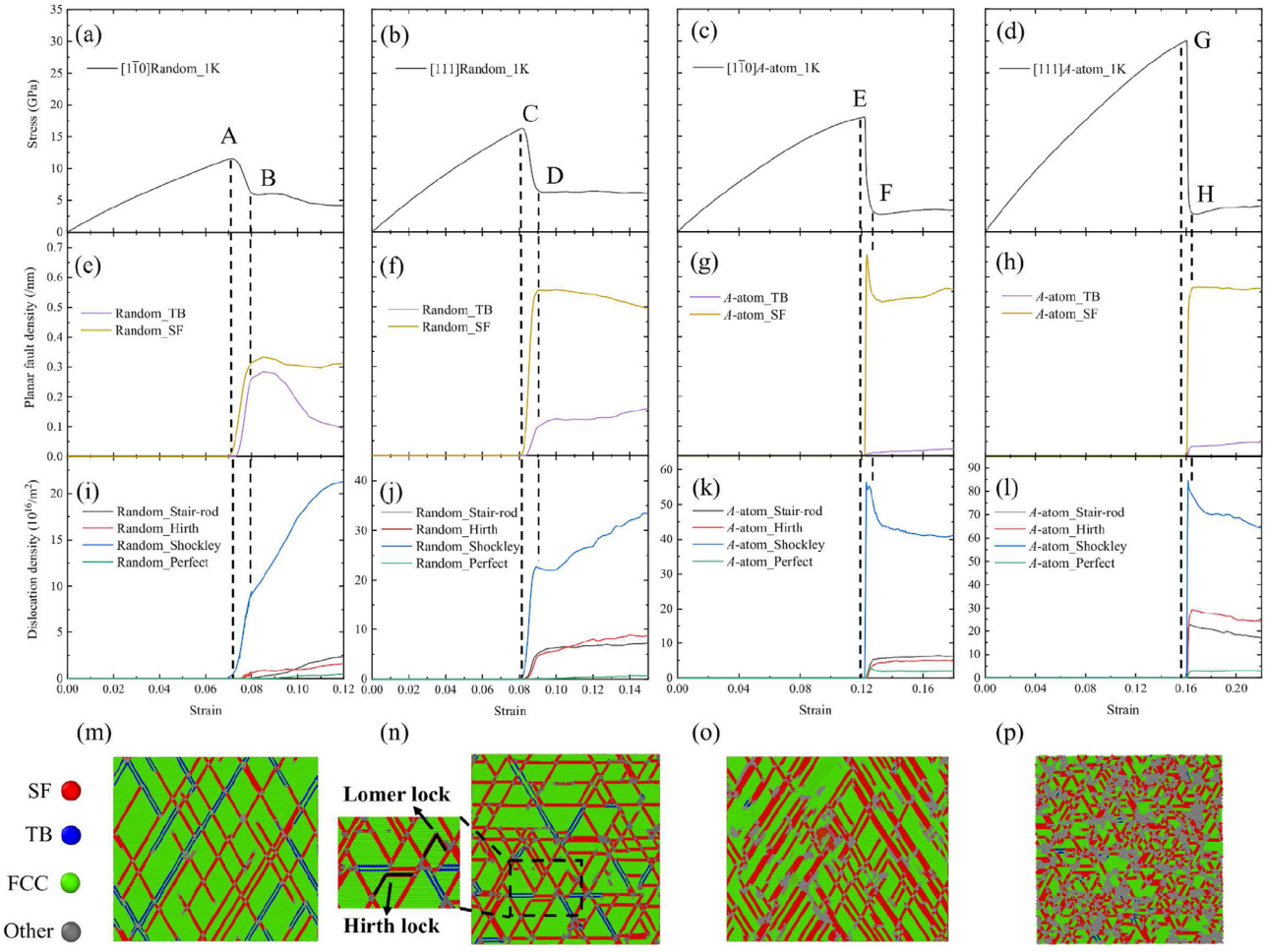

Fig. 4. (a)-(d) Tensile stress-strain curves for the SC random CoCrNi and *A*-atom samples at 1 K deformed along the [1$\bar{1}$0] and [111] crystallographic directions, respectively. The corresponding (e)-(h) planar fault (TB and SF) densities and (i)-(l) dislocation densities as functions of strain, respectively. (m)-(p) The corresponding atomic configurations at points B, D, F and H of stress-strain curves, respectively. Here, the atomic color scheme follows that used in Fig. 1 and the definitions of random and *A*-atom samples are consistent with those in Fig. 2.

cluding Shockley, Hirth, stair-rod and perfect dislocations, occur during tension in the [111] direction than in the [1$\bar{1}$0] direction (Fig. 4(k) versus (l)). This response is similar to that seen in the random CoCrNi sample, as shown in Fig. 4(o) and (p). Compared to the random CoCrNi MEA, the *A*-atom sample generates much more SFs and immobile dislocations (Fig. 4(g),(h),(k) and (l)). This outcome reveals that more dislocation reactions are favored in the early stages of plasticity in the *A*-atom sample than in the random CoCrNi MEA.

In the random MEA test, however, the deformation is accommodated by substantial amounts of nanotwinning (as seen in snapshots at B and D in (Fig. 4(m–n)). In particular, in comparing Fig. 4(e),(m) and (i), we find that more TBs are generated in the sample strained in the [1$\bar{1}$0] direction than in the [111] direction. Evidently LD has aided the formation of nanotwins, even in a conventionally non-twinning orientation. With further straining, nanotwinning in the [1$\bar{1}$0] SC is later followed by detwinning, as indicated by the drop in TB density. In contrast, as strain increases in the [111] SC, detwinning does not occur, but rather stored defect densities increases, giving rise to the observed strain hardening. In this orientation, SPs intersect, react and form Lomer or Hirth locks (as marked by the dash box in Fig. 4(n)), which is evidenced by the high densities of SFs, stair-rod and Hirth dislocations seen in Fig. 4(f) and (j). Lomer and Hirth locks block moving SPs, converting them into immobile dislocations.

When increasing from 1 K to 300 K, the LD in the random MEA has decreased but the thermal vibrations in both the random MEA and *A*-atom have significantly increased, and virtually to the same amount (Fig. 2(f)), making any contributions from LDs existing only in the random material comparatively small. In both the SC *A*-atom and random MEA, the strength drops when going from 1 K to 300 K (Fig. 4(a–d) versus Fig. 5(a–d)). The strength reduction in *A*-atom sample is significant, being $\sim$ 5.0 GPa in the [1$\bar{1}$0] direction and $\sim$ 11.0 GPa in the [111] direction. In contrast, the strength reduction in the random CoCrNi MEA is much smaller, being only $\sim$ 1.8 GPa in the [1$\bar{1}$0] direction and $\sim$ 2.0 GPa in the [111] direction.

Fig. 5 presents an analysis of the underlying glissile and sessile defect densities. Similar to the 1 K response, the peak stresses in the *A*-atom and random MEA response correspond to the strain to first nucleate SPs. Therefore, these two SC materials yield at lower stresses at 300 K compared to 1 K due to the greater ease of first nucleating SPs. The critical strain for SP nucleation in the *A*-atom sample is much lower at 300 K than at 1 K, with reductions of 28.4% in the [1$\bar{1}$0] direction and 38.3% in the [111] direction. As the *A*-atom lacks LD, this reduction implies that the intense atomic thermal vibrations, accompanying the higher temperature, lowered the critical strain for SP nucleation. Thermal fluctuations are known to aid in overcoming the energy barrier for dislocation nucleation. Here, the results indicate that they have a similar effect on SP nucleation as LDs. With the increase in tem-

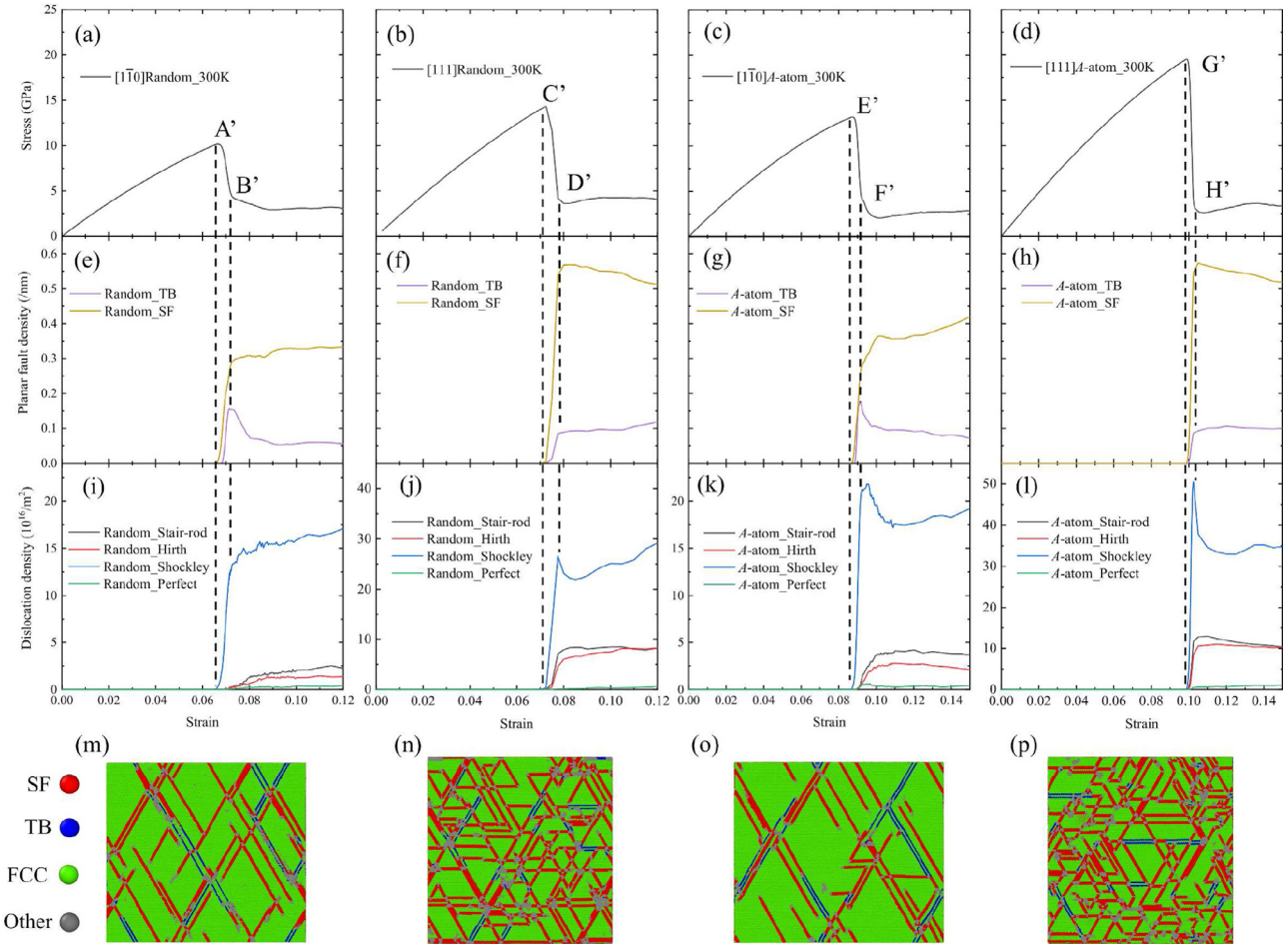

Fig. 5. (a)-(d) Tensile stress-strain curves for the SC random CoCrNi and *A*-atom samples at 300 K deformed along the [1$\bar{1}$0] and [111] crystallographic directions, respectively. The corresponding (e)-(h) planar fault (TB and SF) densities and (i)-(l) dislocation densities as functions of strain, respectively. (m)-(p) The corresponding atomic configurations at points B', D', F' and H' of stress-strain curves, respectively. Here, the atomic coloring follows that used in Fig. 1 and the definitions of random and *A*-atom samples are consistent with those used in Fig. 2.

perature from 1 K to 300 K, the critical strains for SP nucleation in the random CoCrNi MEA remain virtually unchanged or slightly reduced for both the [1$\bar{1}$0] and [111] orientations. Again, it appears that LDs at 1 K are playing a similar role in reducing the nucleation strain as thermal vibrations are playing at 300 K. The net effect is an apparent thermal stability in yield strength of the SC MEA.

With the analysis in Fig. 5, we further examine the SP slip and twinning evolution after yield at 300 K. For reference, in the *A*-atom sample, the relative contributions of nanotwinning compared to SP glide have nearly doubled at the higher temperature. For the random CoCrNi MEA, however, the mechanisms have not changed significantly from those at 1 K. Second, at 300 K, both the *A*-atom and random MEA have similar evolution in deformation mechanisms with straining beyond yield. They both deform by SP glide and nanotwinning for the same test direction. Considering there is no LD but only thermal vibrations in the *A*-atom sample at 300 K, the similarity between the random MEA and pure metal *A*-atom further supports the notion that atomic thermal vibrations and LD play similar roles in encouraging nanotwinning and slip by SPs.

With calculation of the SP and SF density evolution, we estimate the average speed of the SP dislocations (see Appendix C). Fig. 6 shows the average speed in the initial stages of straining in the [1$\bar{1}$0] SCs at 1 K before prevalent lock formation accumulates. Comparing the *A*-atom and random MEA SCs indicates that LD has slowed down SP motion. A similar finding was reported in [40,55].

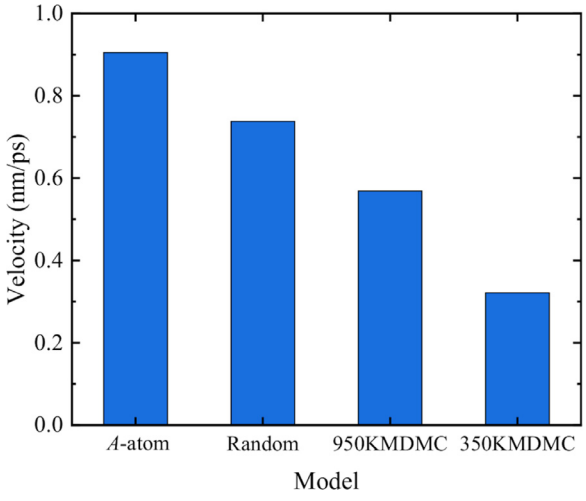

Fig. 6. The average speed of SP dislocations in *A*-atom and various CoCrNi SC samples with tension along [1$\bar{1}$0] direction at 1 K.

3.1.4. Nanotwin nucleation and detwinning mechanisms

The mechanisms for forming nanotwins in the [111] *A*-atom SC and two MEA SC orientations are found to be the same. They all initiate by dislocation slip [85], explaining why nanotwins appear

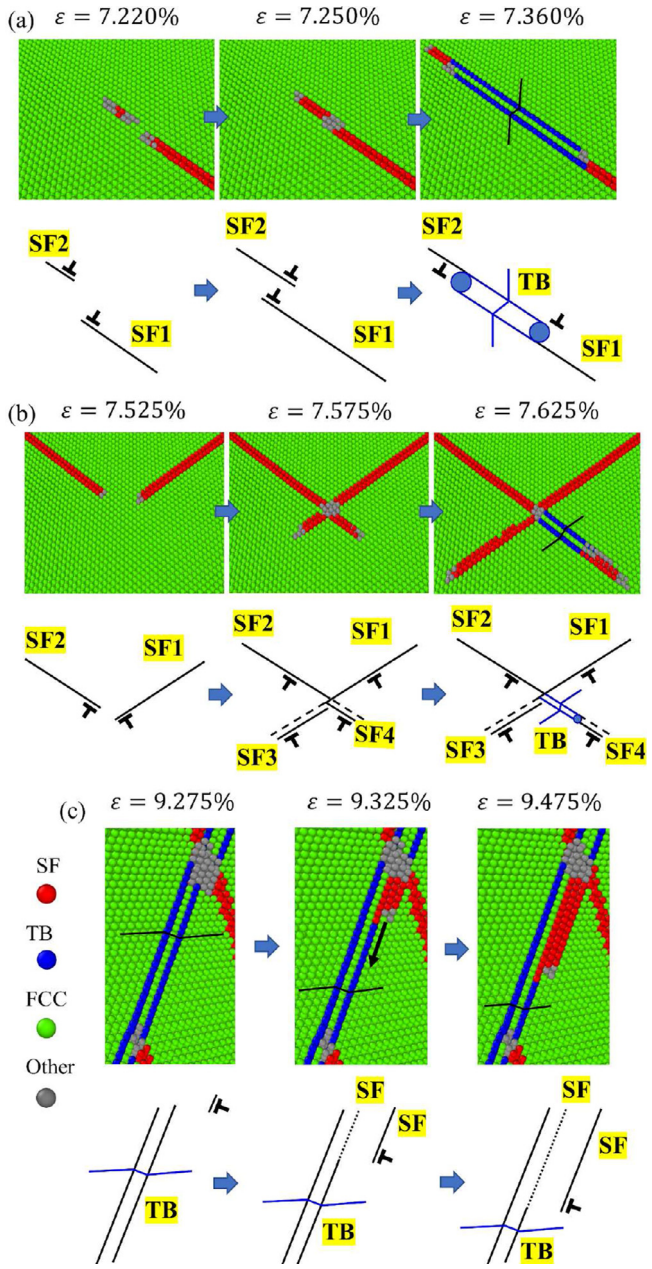

Fig. 7. (a)-(b) Atomic configurations and the corresponding schematics for nanotwinning. (c) Atomic configurations and the corresponding schematic for detwinning. The atomic coloring follows Fig. 1.

only after the peak stress and after some amount of SPs have propagated. One mechanism involves the formation of a two-layer twin via the glide of two SP dislocations propagating on two parallel and adjacent glide planes. They can glide in either the same or opposite directions [86–88]. Fig. 7(a) shows an example of the latter mechanism seen in the random MEA SC. Following SP dislocation ($\epsilon = 7.220\%$), each SF has two atomic layers and these two neighboring SFs (SF1 and SF2) span three atomic layers. Once the SPs overlap each other ($\epsilon = 7.250\%$), the middle atomic layer becomes faulted twice, transforming back to FCC stacking. In this way, a twin with two TBs is formed ($\epsilon = 7.360\%$). Another mechanism for nanotwinning seen here (Fig. 7(b)) involves the intersection of two SPs initially gliding on non-parallel planes ($\epsilon = 7.525\%$). After intersecting, their glide planes change by one atomic layer, while maintaining the original glide direction ($\epsilon = 7.575\%$). A nanotwin is then seen to nucleate at the intersection point ($\epsilon = 7.625\%$).

We further analyze the process of detwinning, an unusual occurrence observed only in the random MEA $[1\bar{1}0]$ tests. Fig. 7(c) shows a series of snapshots in strain of the detwinning process. The process begins with the SF left by a mobile SP intersecting with a propagating nanotwin ($\epsilon = 9.275\%$). At their intersection point, another SP nucleates and propagates on a plane adjacent to the nanotwin's TB ($\epsilon = 9.325\%$). As the SP glides, the twin transforms into a SF stack of three atomic layers with HCP-stacking ($\epsilon = 9.475\%$). Thus, frequent interactions between SPs and nanotwins during deformation led to transformations of nanotwins into HCP phase nano-ribbons.

After point B in the stress-strain curve along the $[1\bar{1}0]$ loading direction (Fig. 4(e)), the total planar fault density begins to drop, finally reaching 0.41 nm^{-1}, a consequence primarily of detwinning (i.e., the drop seen in TBs from 0.25 nm^{-1} to 0.10 nm^{-1}). Detwinning evidently overwhelms nanotwinning in the later stages of plasticity. As demonstrated in Fig. 7(c), detwinning originates from the interaction between nanotwins and SP dislocations. Because there is little immobile dislocation density to block their motion, SP dislocations can move easily, as seen by the rapid increase in SP density of 21.0×10^{16} m^{-2}. Fast-moving and proliferating SPs increase the likelihood of nanotwin intersections and, thus, detwinning. In contrast, in the [111] orientation test, the planar fault densities stabilize, as seen in Fig. 4(f) by the slight decrease in SFs and increase in TBs. Abundant Lomer and Hirth locks develop in the early stages, impeding SP motion, decreasing their probability of interacting with nanotwins, and suppressing detwinning. Such results are consistent with recent experimental observations in CoCoNi MEA, reporting higher ductility in the $[1\bar{1}0]$ test but higher strength in the [111] test [23].

3.1.5. The effect of CSRO on the tensile deformation

To distinguish the effects of CSRO from LD, we analyze and compare the mechanisms controlling the deformation responses of the random CoCrNi, with no CSRO, and two other CoCrNi samples, the 950KMDMC and 350KMDMC samples, with differing levels of CSRO. Among these three MEAs, LDs are also present but their average LDs are nearly the same (Fig. 2(f)).

Fig. 8 (a–b) display the tensile stress-strain curves of the different SC CoCrNi samples at 1 K and two $[1\bar{1}0]$ and [111] orientations. Comparing the three responses shows that the peak stress increases with increasing degree of CSRO (Fig. 8(e)). In all three MEAs, the peak stress corresponds to the strain at which SPs nucleate and propagate. Prior to reaching the peak stress, the material is then elastic. Comparing the elastic responses of all three MEAs indicates that with larger values of CSRO, the larger the Young's modulus and critical strain to nucleate SPs. Further, the 350KMDMC sample has the highest peak stress, because it exhibits the highest Young's modulus and strain to first nucleate SPs.

Figure S1 in the supplementary material shows the same set of SC curves at the higher temperature 300 K, a change that raises the thermal vibration in all samples equally, while retaining the same levels of CSRO. The SC response at higher temperature is similar to that at 1 K and the 350KMDMC sample maintains the highest stress among the three MEAs. Evidently, large values of CSRO increase the resistance to first nucleate SPs relative to a random MEA with no CSRO.

Figure S2– S5 in the supplementary material presents an analysis of the corresponding evolution in the SF and TB densities and mobile SP and dislocation densities as functions of strain. After the peak stress is reached, the stress drops and continued deformation is accommodated by SPs and nanotwinning. The relative amounts of SP glide compared to twinning are similar among the three MEAs. In the [111] SC test, SP glide is the dominant de-

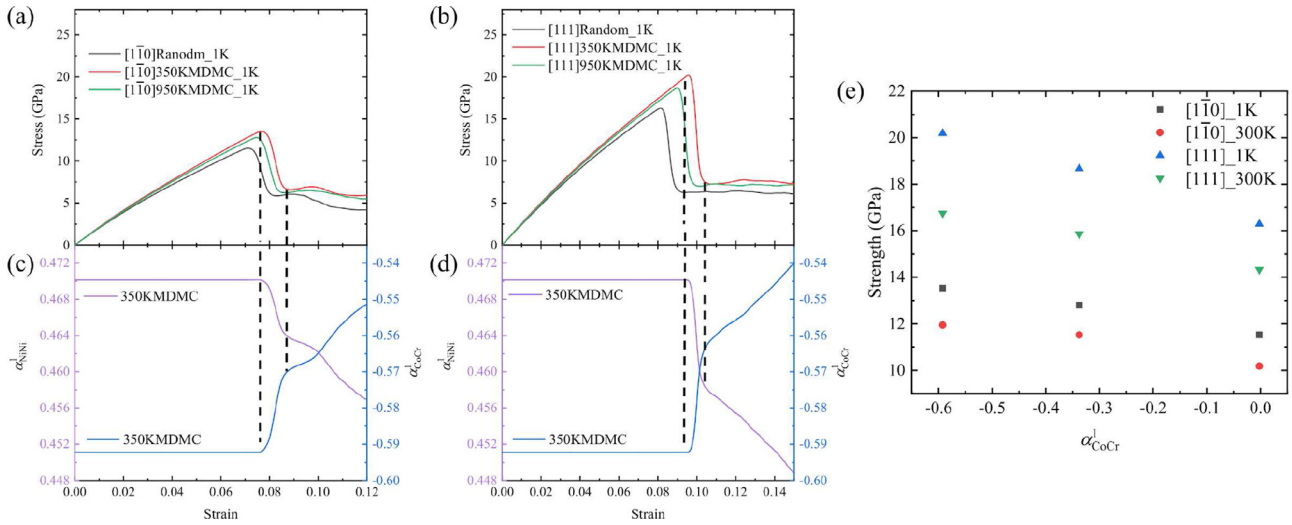

Fig. 8. (a)-(b) Tensile stress-strain curves for various SC CoCrNi samples at 1 K deformed along the [1$\bar{1}$0] and [111] crystallographic directions, respectively. (c)-(d) The corresponding pairwise CSRO parameters α^1_{NiNi} and α^1_{CoCr} of 350KMDMC SC CoCrNi sample as functions of strain along the [1$\bar{1}$0] and [111] crystallographic directions, respectively. (e) The ultimate strengths for SC CoCrNi samples as functions of α^1_{CoCr} at 1 and 300 K when deformed along the [1$\bar{1}$0] and [111] crystallographic directions, respectively. Here, the definitions of 350KMDMC, 950KMDMC and random samples follow Fig. 2.

formation mechanism, whereas in the [1$\bar{1}$0] SC test, SP and nanotwinning both contribute to post-yield deformation. In the later stages of straining, detwinning occurs. These mechanisms are unchanged with the change in the degree of CSRO among the random, 950KMCMD and 350KMCMD samples. These results confirm that the higher levels of CSRO resist the nucleation of SPs at yield.

In Fig. 8(c–d), we also trace the evolution of the pairwise CSRO parameters α^1_{CoCr} and α^1_{NiNi}. We observe that the degree of CSRO starts to change when the peak tensile stress is reached and SPs nucleate and propagate. The evolution involves an increase in α^1_{CoCr} and decrease in α^1_{NiNi} (Fig. 8(c–d)), essentially reducing the strength of the CSRO as straining proceeds. The net effect of the glide of SPs is to shift the original atomic neighbors and randomize the elemental pairs. In the interest of space, only the 350KMDMC case is shown and the results for the random and 950KMDMC samples can be found in Figure S6 of the supplementary material.

Prior works have reported that CSRO helps enhance tensile strength. The viewpoint is that strengthening results from the higher energy costs in moving dislocations through or breaking them away from the large-value CSRO regions [55]. The higher strength SC with higher degrees of CSRO seen here are, however, different. We show, and isolate from LD effects, that increased levels of CSRO enhance the Young's modulus and increase the critical strain to SP nucleation, leading to the enhancement in yield strength.

To further reveal the role of CSRO on dislocation nucleation, we use the crystal analysis method to identify the locations where SPs typically first nucleate in each of these cases. The deformation snapshots for various CoCrNi samples at the moment of dislocation nucleation are also displayed in the middle column of Fig. 9. For better visualization, only atoms with $\alpha^1_{CoCr} < -0.8$ and SF atoms are shown in purple and red, respectively. Among all three CoCrNi MEAs, SPs initiate within the CoCr clusters and then propagate across the crystal.

To determine why the SPs prefer to originate in the CoCr clusters, we correlate the shear strains that develop across the crystal with the local value of the CSRO. Fig. 10 shows the atomic shear strains in one cross-section of the 350KMDMC SC CoCrNi sample in (a) [89], alongside maps of the pairwise CSRO parameters α^1_{NiNi} and α^1_{CoCr}, (in (b)–(c)). The shear strain distributions are inhomogeneous and diffuse, since the atomic shear strains are affected by thermal fluctuations and the dynamically changing atomic velocities, unlike the CSRO maps, which use stationary atomic positions. Nonetheless, a closer look at some of the local regions with large shear strains (see insets), are associated with more negative α^1_{CoCr} or less positive α^1_{NiNi}, suggesting atomic strains concentrate in the CoCr-ordered clusters rather than in the Ni-rich regions. Repeating the analysis for other cross-sections and the 950KMDMC and random CoCrNi MEAs reveals the same correlation, see Figure S7 and S8 of the supplementary material. Figure S9 shows the GSFE $\{111\}<112>$ curves for the random MEA, random CoCr mixture and pure Ni. Comparing their unstable SFE indicates that it is easier to form the faults in the CoCr and hardest in the Ni. With higher levels of CRSO, the CoCr clusters are more likely to be surrounded by Ni, making it harder for the SPs to propagate away from the CoCr nucleation sites.

Like LD, CSRO appears to also resist the glide of SP dislocations. Fig. 6 compares the average SP speed between the *A*-atom and two MEAs with lower degrees (950KMDMC) and higher degrees of CSRO (350KMDMC). The average speed decreases, not only with the introduction of CSRO, but also with increases in the value of CSRO.

3.2. Nanocrystalline MEA

3.2.1. The stress-strain curves and the ultimate strength

Fig. 11 (a) shows the calculated tensile stress-strain curves at 1 K for three NC materials, the CoCrNi with CSRO (350 K), the nominally random CoCrNi, and the *A*-atom pure material. As a marked distinction from the SCs, the *A*-atom NC material is the weakest among all three NC materials. Once again, however, the strength of the NC CoCrNi with the higher degree of CSRO is greater than the random NC CoCrNi. Fig. 11(b) shows the tensile stress-strain curves for the same three NC materials but at 300K. The rank order still persists with the CSRO NC CoCrNi providing the highest strength, followed by the random NC CoCrNi and the pure *A*-atom NC material yielding the weakest strength. The *A*-atom material contains no LD and the MEA has significant LD at 1 K but negligible LD at 300 K (Fig. 2(f)). Apparently, the LD was not the factor that distinguishes their strength.

Within the same plots in Fig. 11(a-b), we also present the tensile deformation responses for the material with pre-existing nan-

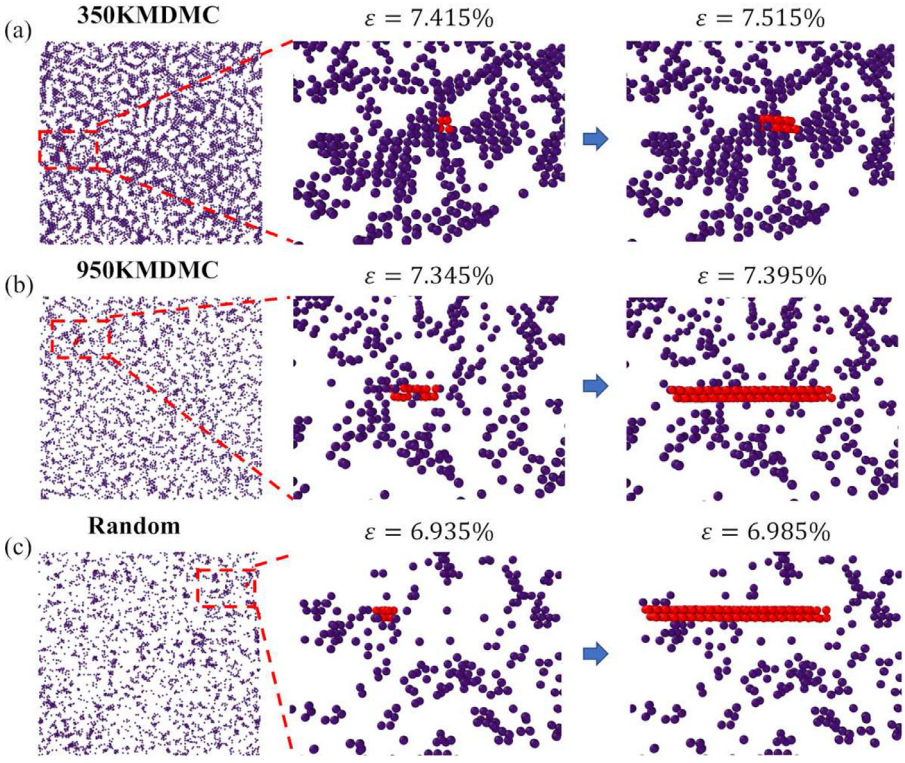

Fig. 9. (a)-(c) Configurations of 350KMDMC, 950KMDMC and random SC CoCrNi samples under uniaxial tension at 1 K, respectively. Only atoms with $\alpha^1_{CoCr} < -0.8$ and SF atoms with hexagonal close-packed (HCP)-like coordination are shown in purple and red, respectively. Here, the definitions of 350KMDMC, 950KMDMC and random samples follow Fig. 2. (For interpretation of the references to colour in this figure legend, the reader is referred to the web version of this article.)

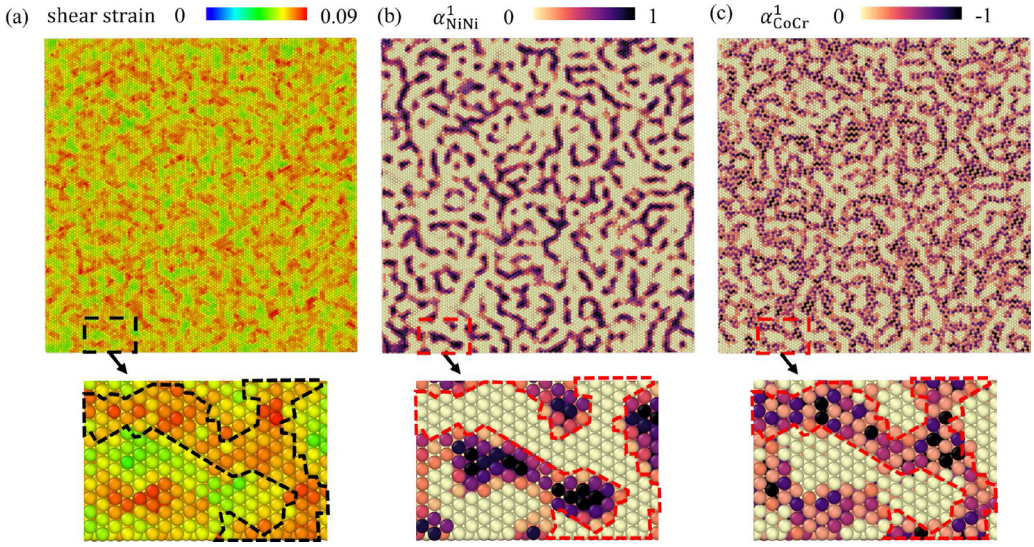

Fig. 10. The configuration of 350KMDMC SC CoCrNi sample at the tensile strain of 0.075 and the temperature of 1 K. (a)-(c) The atoms are colored according to the atomic shear strain, pairwise CSRO parameters α^1_{NiNi} and α^1_{CoCr}, respectively. More positive valued α^1_{NiNi} and more negative valued α^1_{CoCr} means stronger CSRO. Here, the definition of 350KMDMC follows Fig. 2.

otwins and ISFs. As would be expected, subgranular ISFs or TBs result in higher strengths than without. Compared to the material free of subgranular boundaries, strength enhancements range from 3.42% to 7.18% for the ISFs and from 6.09% to 10.40% for the TBs. Together, large values of CSRO and pre-existing subgranular nanotwins provide the highest strengths.

In Fig. 12, we analyze the strain evolution of deformation mechanisms of the 350 K CSRO CoCrNi NC samples both without and with pre-existing densities of subgranular ISFs and TBs. For the NC material without initial TBs or ISFs, the analysis identifies macro yielding with the initiation of SPs and relatively minute perfect dislocation activity. The motion of the partials leads to immediate formation of SFs. With further straining beyond the peak stress, SPs continue to propagate and SFs and nanotwins continue to form, and the material macroscopically softens. We also see that glide by perfect dislocations and accumulation of sessile dislocation storage begins after the peak stress is reached and remains minimal for the remainder of the straining period. In particular, a considerable number of TBs is generated, reaching a density of 0.12 nm^{-1} after the strain of 0.15. Accompanying the SF increase, the densities of

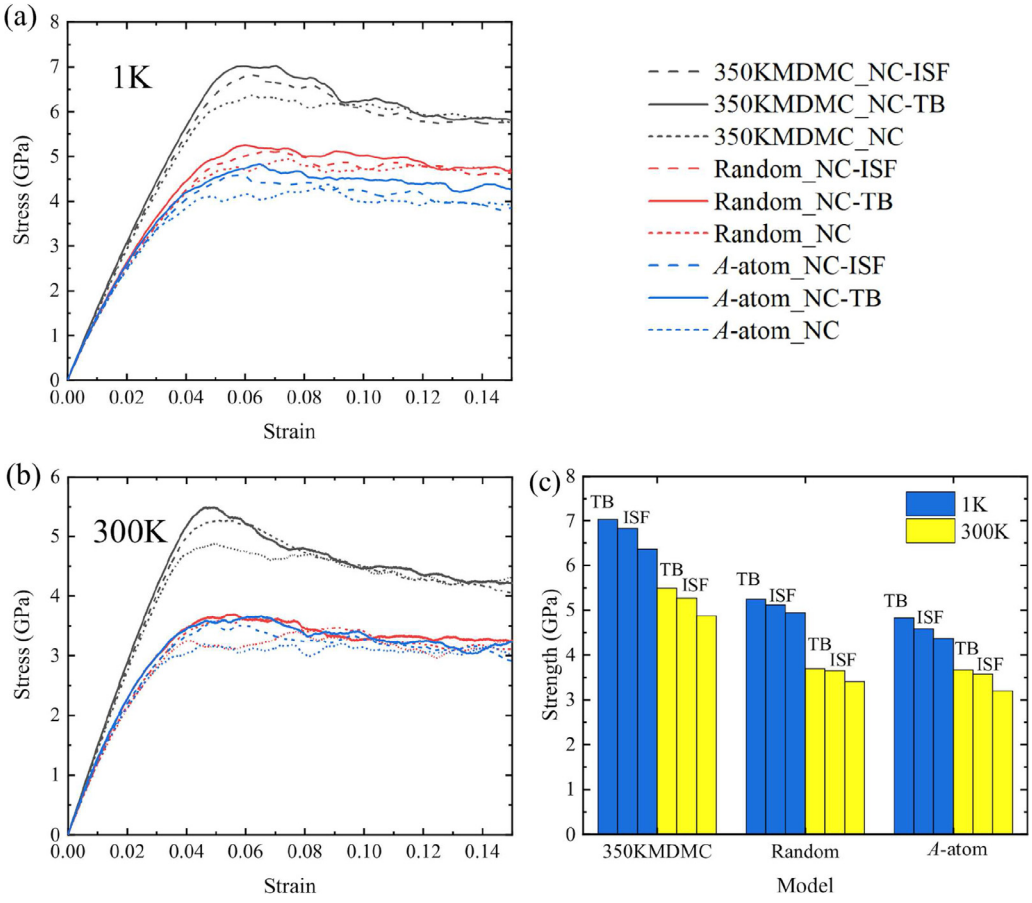

Fig. 11. Tensile stress-strain curves for the NC samples at (a) 1 and (b) 300 K. (c) The ultimate strengths for the NC samples at 1 and 300 K, respectively. Here, the definitions of 350KMDMC, random and *A*-atom follow Fig. 2. TB and ISF denote NC samples with the TBs and ISFs inserted, respectively.

various other defects rise (Fig. 12(g)), reaching a total density of $\rho = 5.0 \times 10^{16}$ m^{-2}, with 80% contributed by SP dislocations. The sequence of SFs and followed by TBs is similar to the deformation process the SC CoCrNi sample (Fig. 4(e–f)). For NC material with pre-existing ISFs (Figure c), yielding appears to be associated with simultaneous formation of mobile SPs and nanotwins. As the material is strained past yield, it hardens to the peak strength and then softens. Underlying this response, both SPs and nanotwin densities continue to rise. In contrast, for the MEA with initial subgranular TBs (Figure b), yielding occurs at the moment when SPs move. After yield, we observe the formation of SFs and detwinning of the pre-existing nanotwins. The densities of mobile SPs generated during straining are much higher than those generated during deformation of the NC material free of subgranular boundaries and the other one containing ISFs.

Performing the same analysis on the random MEA and pure NC *A*-atom material finds similar deformation mechanisms and sequences and similar effects of ISFs and TBs. Generally, yield in these NC alloys occurs by the nucleation of mobile SPs from the GBs and strain hardening after yield is associated predominantly with SP motion and nanotwinning. These pre-existing subgrain boundaries are not arbitrary boundaries but the same boundaries that would be generated by the two predominant mechanisms operating in this MEA, SFs and TBs. The shared outcome of these deformation mechanisms, however, do not readily explain why the MEA material with CSRO studied in the foregoing analysis proved to have the highest NC strengths at both 1 K and 300 K. Further, it is not clear how the pre-existing subgranular TBs can strengthen the NC alloy, while at the same time cause detwinning with straining.

3.2.2. Nucleation of mobile partials and nanotwins

To address these issues, we used the crystal analysis method to determine where in the nanostructure these mechanisms formed and propagated. Fig. 15 compares snapshots of 350KMDMC_NC, 350KMDMC_NC-ISF and 350KMDMC_NC-TB samples during tension at the strain of 10%. Analysis reveals that all NCs first form mobile SPs at the GBs before the peak stress is reached. Fig. 15(a) shows that a partial dislocation that has been activated from the GB can reach the opposite GB unhindered (marked by a white arrow).

First, we consider the deformation response of the NC samples without subgranular TBs and ISFs. When strain is applied to the *A*-atom_NC sample, numerous SPs emit from the GBs and move rapidly, forming SFs across the crystals. In the 350KMDMC_NC sample, SPs also emit from the GBs, but preferentially where the CoCr lie. As an example, Fig. 13(a) shows, over a series of increasing strain levels (3.170% to 4.310%), the nucleation and motion of an SP in this sample. To expose these defects, the perfect FCC atoms have been removed from the image. In Fig. 13(a), a SP is seen emitting from an ordered CoCr cluster at the GB, as marked by white arrows. As the analysis of the SC samples in Fig. 9 revealed, the larger the degree of CoCr CSRO, the higher the strain required to emit SPs from them. The 350KMDMC_NC samples, therefore, can be expected to be stronger than the *A*-atom_NC and random NC MEA samples, since CoCr clustering at the GBs makes nucleation of SPs more difficult.

In addition, in the initially ISF- and twin-free NCs, nanotwinning is seen to occur after yield, via mechanisms that are the same as those occurring in the SCs (Fig. 7(a–b)). Fig. 13(b) shows an example of twin nucleation in the 350KMDMC NC. SPs, nu-

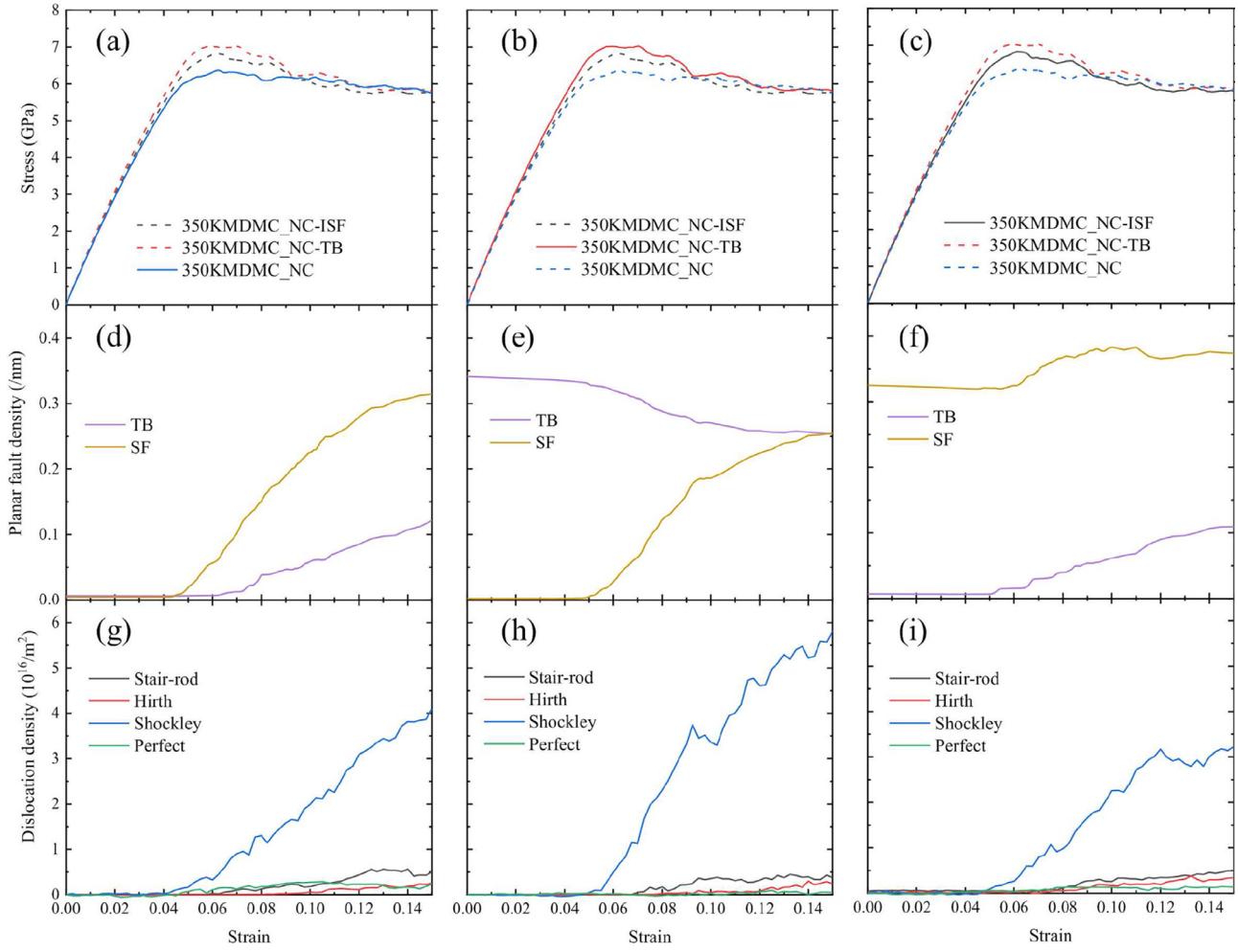

Fig. 12. (a)-(c) Tensile stress-strain curves for 350KMDMC_NC, 350KMDMC_NC-TB and 350KMDMC_NC-ISF samples at 1 K, respectively. The corresponding (d)-(f) planar fault (TB and SF) densities and (g)-(i) dislocation densities as functions of strain, respectively. The definitions of 350KMDMC, TB and ISF follow Fig. 11..

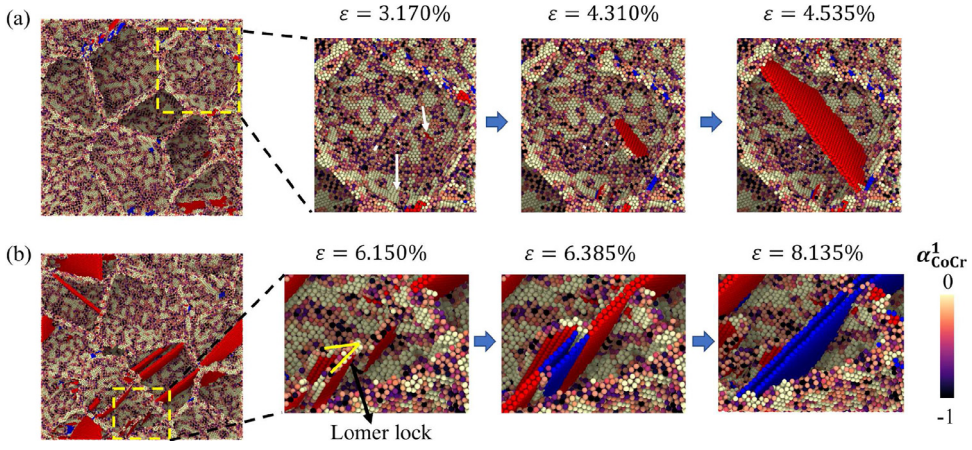

Fig. 13. Nucleation and development of (a) dislocations and (b) nanotwinning in 350KMDMC_NC sample during tension at 1 K. FCC atoms have been removed to better visualize the dislocations, planar faults and grain boundaries (GBs). SF and TB atoms are colored by red and blue, respectively. Except SF and TB atoms, GB atoms are colored according to α^1_{CoCr}. The definition of 350KMDMC_NC follows Fig. 11. The white arrows at $\epsilon = 3.170\%$ in (a) denote the Shockley partial dislocation nucleation sites and the yellow lines at $\epsilon = 6.150\%$ in (b) highlight the Lomer lock. (For interpretation of the references to colour in this figure legend, the reader is referred to the web version of this article.)

cleating at the GBs, glide along multiple, non-planar systems, causing them to intersect (see highlighted by yellow lines at $\epsilon = 6.150\%$). The intersection points serve as sources for nanotwins (e.g., $\epsilon = 6.385\%$), which then glide across the grain (e.g., $\epsilon = 8.135\%$).

3.2.3. The effect of pre-existing subgranular stacking faults and twins

Fig. 15 (b) shows the defect evolution in a set of grains within the 350KMDMC_NC-ISF sample containing pre-existing subgranular ISFs. SPs forming from the GBs are hindered by the ISFs (as marked by A, B and C). After cutting through the ISFs, the SPs deviate from

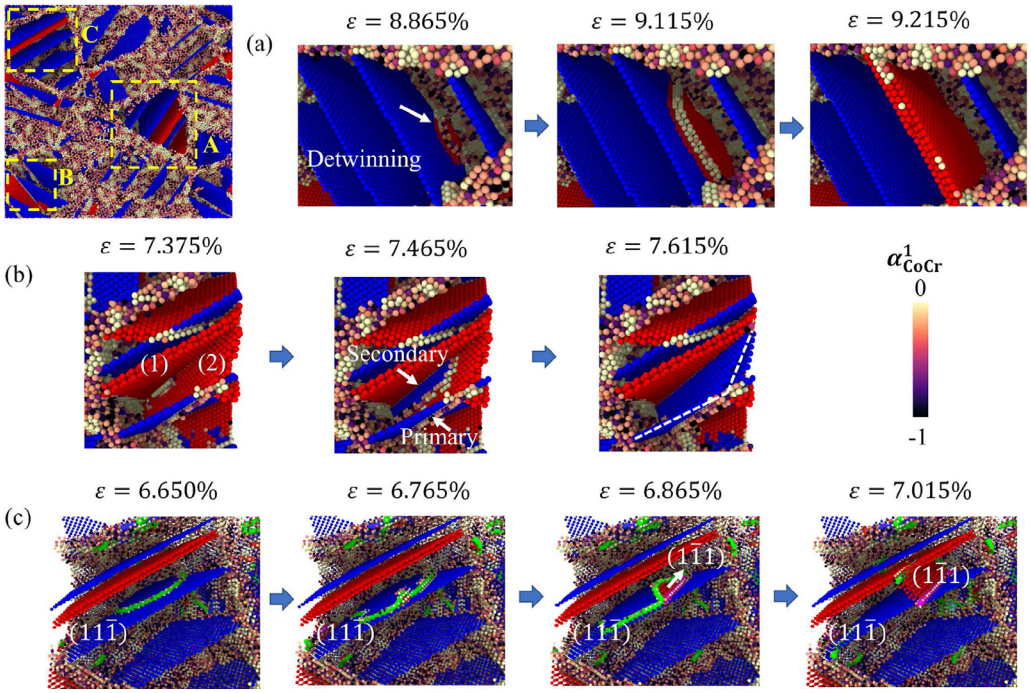

Fig. 14. The evolution of (a) detwinning, (b) three-dimensional (3D) nanotwin network structure and (c) Lomer lock in 350KMDMC_NC-TB sample during tension at 1 K. The definition of 350KMDMC_NC-TB and the atomic coloring follow Fig. 11 and Fig. 13, respectively. (a), (b) and (c) correspond to regions A, B and C, respectively. In (b), white arrows at $\epsilon = 7.465\%$ and white dash lines at $\epsilon = 7.615\%$ highlight the primary and secondary nanotwins. To aid visualization in (c), various dislocation types are distinguished by different colors.

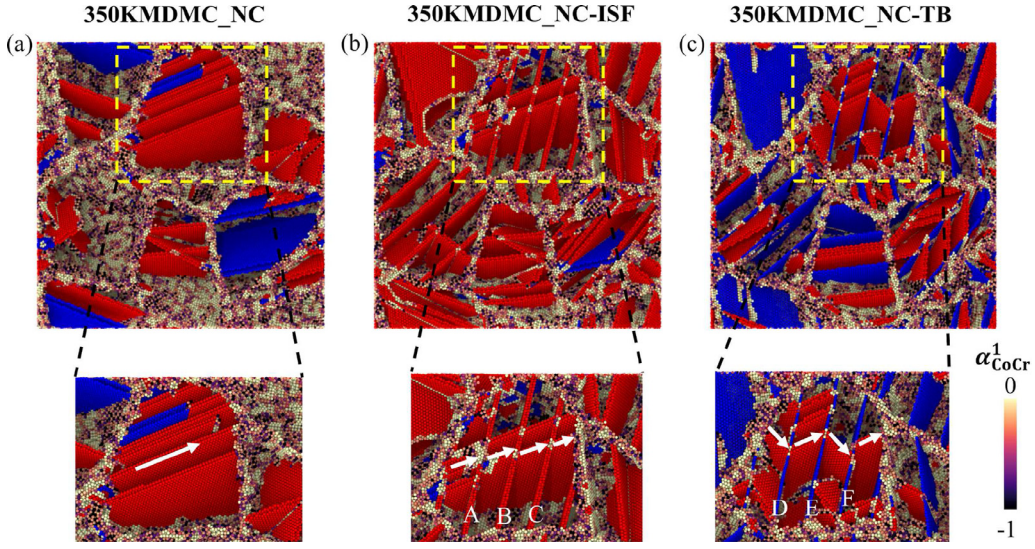

Fig. 15. The snapshots of (a) 350KMDMC_NC, (b) 350KMDMC_NC-ISF and (c) 350KMDMC_NC-TB samples at 1 K and the tensile strain of 10%. The definitions of 350KMDMC_NC, 350KMDMC_NC-ISF and 350KMDMC_NC-TB samples follow Fig. 11, while the atomic coloring follows Fig. 13. A, B, and C in (b) denote the inserted ISFs. D, E and F in (c) represent the inserted TBs.

their original glide planes. The increase in the density of SFs and twins generated by the moving SPs is similar or even lower than those of the NC sample without pre-existing ISFs (Fig. 12(f) and (i)). Evidently, introducing subgranular ISFs do not promote or delay emission of SPs and the enhanced strength results from the interactions between the pre-existing ISFs and the mobile SPs.

Fig. 15 (c) analyzes the defect evolution in the NC with pre-existing twins. Unlike the NC with pre-existing ISFs, the motion of the SPs is completely blocked by the pre-existing TBs (marked by D, E and F in Fig. 15(c)). New SPs are generated at these intersections and they glide along the mirror plane according to the TB, (as shown by white arrows), forming a zigzag ISF structure. We find that the TBs also provide planes on which SPs from the GBs can glide. Fig. 14(c) shows an SP, which is in this case a twinning partial, gliding on the (11$\bar{1}$) TB plane at 6.650% strain and resulting in TB migration. Eventually it interacts with another partial dislocation gliding on the (1$\bar{1}$1) plane at 6.865% strain, forming the Lomer lock. Finally, the SP, from one side of the newly formed Lomer lock, intersects another SF at a strain of 7.015%, resulting in the creation of a SF network. Thus, the TBs, by diverting the glide path of the SPs and providing planes on which SPs can glide as twinning partials, promote the formation of SPs and SFs. As a result, the highest rates of SP and SF density evolution occur in the NC with pre-existing subgranular twins. We note that TEM analyses on CoCrNi MEA [25] observed similar events of twinning and multi-planar slip at cryogenic temperatures and had proposed them to be linked to the remarkably good ductility of this MEA at cold temperatures.

At the same time, in the 350KMDMC_NC-TB sample, for instance, we observe detwinning of the pre-existing twins with straining, as suggested by the reduction in TB density from $0.34\,nm^{-1}$ at 0.05 strain to $0.25\,nm^{-1}$ at 0.15 strain (Fig. 12(e)). Analysis of the dynamics within the nanocrystals confirms that the reduction in TB density is associated with detwinning in some grains (Fig. 14(a)), via the same process as detailed in Fig. 7(c). Initially ($\epsilon = 8.865\%$ in (a)), an SP, denoted by the white arrow, is emitted from the GB on a plane adjacent to the TB, leaving behind an SF containing two atomic layers adjacent to the TB plane. As the SP extends, the SF that is created in its wake transforms the neighboring TB atoms into SF atoms ($\epsilon = 9.115\%$), resulting in a new SF structure with three atomic layers ($\epsilon = 9.215\%$). This transformation of pre-existing TBs to SFs also contributes to the rise of the SF density (Fig. 12(e)).

In most of the grains, the pre-existing TBs are removed leading to a net reduction in TBs, yet in a small number of grains, a three-dimensional (3D) nanotwin network forms. Fig. 14(b) demonstrates the formation of one such network by the intersection of non-parallel nanotwins in the same grain. SP dislocations in different slip systems, followed by SFs, can be activated during tension. Some of the SFs are parallel to the inserted TBs (e.g., (1) at $\epsilon = 7.375\%$), while others are not (e.g., (2) at $\epsilon = 7.375\%$). The intersections in the latter grains can give rise to secondary nanotwins, non-parallel to the initial TBs (white arrows at $\epsilon = 7.465\%$). As a result, a 3D nanotwin network forms, as highlighted by the white dash lines ($\epsilon = 7.615\%$). We note that 3D nanotwin networks were also reported from an experimental study on deformed CoCrNi [18]. To summarize, the differences between the SP/ISF and SP/TB interactions taking place in the nanocrystals after yield explain why the NC with pre-existing twins (350KMDMC_NC-NT) has the highest strength. These results suggest that pre-straining the NC to introduce TBs could help to further strengthen CoCrNi MEAs.

3.3. Discussion

In this work, we tested many forms of MEAs, –SCs and NCs, and random samples and samples with CSRO–at two deformation temperatures, 1 K and 300 K. The MD simulations here are used to provide insight into the relationship between LD and CSRO on the underlying mechanisms of deformation. Due to the limited time and length scales inherent to the approach, the strain rates, stresses, and dislocation densities will be much higher than realized experimentally. In the typical quasi-static loading condition used in experimental studies, involving for instance CoCrNi MEA [28], CoCrFeMnNi HEA [90] and AlCoCrFeNi HEA [91], the dislocation densities range from 10^{13} m^{-2} to 10^{15} m^{-2} at the strain rate of 10^{-4} $s^{-1} \sim 10^{-3}$ s^{-1}. In contrast, in the present calculations, the dislocation densities generated under a strain rate of 5×10^{8} s^{-1} lie in the range from 10^{16} m^{-2} to 10^{17} m^{-2}. Further, actual materials contain internal, pre-existing defects, whereas the starting crystals in the current simulations are perfect. With the high strain rates in combination with the defect-free initial state, the stresses reached in simulation cannot be possibly achieved experimentally. Here, we focus on the mechanisms explaining how changes in LD and CSRO would affect the evolution of stress and defect densities, and, as discussed below, we find that the calculated results shed light on observations reported on CrCoNi and other FCC MEAs and HEAs.

Compared to the pure *A*-atom reference material, the MEAs exhibited better stability with respect to elevated temperatures in their critical dislocation nucleation strain and their yield strength. Many experimental studies have reported outstanding thermal stability in mechanical properties in this and other MEAs and HEAs [1,92,93], and have generally attributed it to high mixing entropy and sluggish diffusion or phase decomposition, which are all characteristic of MEAs and HEAs [94]. However, due to the difficulties in studying diffusive dynamics in the very limited time scale of MD simulation, the thermal stability seen here has a different origin. In SC MPEAs, without the presence of GB sources, we find that LD reduces the strain to nucleation, in a similar way that thermal vibrations lower strains to nucleation. Thus, when thermal vibrations increase and LDs decrease with increases in temperature, the net effect on the strain to nucleation in the MPEA is similar. In contrast, in the pure metal with no LD, going from little to no thermal vibrations at low temperature to increased thermal vibrations at elevated temperature detrimentally lowers the nucleation strain.

LD has been associated with increasing the resistance to dislocation glide [40]. Here we reveal that LD has an unusual effect of also lowering the Young's modulus and the strain to nucleation within perfect SCs. Without grain boundaries or internal defects to provide easy nucleation sites for dislocations, MEA SCs with LD will produce dislocations at lower strains and stresses than a SC without LD, such as the *A*-atom SC. When the yield strengths of the SC samples are determined by the stress to first nucleation of dislocations, the *A*-atom SC sample, therefore, will have the highest strength above all the MEAs (see Fig. 3). LDs, however, do not lower the SP nucleation strain below that from GBs. Consequently, in NCs, the effect of LD on propagation, and not on dislocation nucleation, is realized, and we observe that MEA NCs are stronger than *A*-atom NCs (Fig. 11(c)).

Another interesting phenomenon often reported from experimental and modeling studies of FCC MEAs is the prevalence of nanotwinning. For the same orientation, the MEA SCs form much higher fractions of nanotwins (higher density of TBs) compared to the *A*-atom SC. The extent of nanotwinning in the MEA is so prevalent that even the orientation-dependent competition between slip and twinning, common in pure FCC metals, is altered. It is expected in FCC metals that tension in the $<111>$ direction favors twinning, whereas tension in the $<110>$ direction favors slip, since the former stress state promotes widening of extended dislocations as the stress increases [69–73]. The *A*-atom SC exhibits this conventional orientation-dependence, with little nanotwin formation in the $<111>$ direction and nearly none in the $<110>$ direction. However, more twins are generated in the random CoCrNi MEA SC when the sample is tested in the $<110>$ direction than in the $<111>$ direction (Fig. 4(e) versus Fig. 4(f)). This anomalous behavior is also observed by the tensile experiments of the SC CoCrNi MEA [23], where nanotwinning was prominent in the $<110>$ tensile test, while dislocation slip and nanotwinning prevailed in the $<111>$ tensile direction.

Direct comparisons of the SC responses of the CoCrNi MEA with the *A*-atom reference metal at 1 K demonstrates that LD plays a key role in promoting nanotwinning in the MEA after yield and throughout the straining period. LD does not alter the mechanisms of twinning from those understood for pure FCC crystals. Instead LD encourages twinning over SF formation by lowering the strain for SP nucleation, while at the same time increasing their resistance to propagation. In the *A*-atom SC, the [111] suitable orientation for twinning promotes SP nucleation, whereas in the MEA SC, LD promotes it in both orientations. In the [111] orientation, in the *A*-atom material, after nucleation, the SPs move with little resistance and on multiple, non-coplanar glide planes homogeneously throughout the SC. In the MEA under [111] tension, SPs nucleate also on multiple planes, but more profusely, and afterwards move slower, increasing the chances for twinning. The frequent SP intersections on non-coplanar planes for this orientation also gives rise to sessile dislocation structures, characterized by the large number of Lomer and Hirth locks in Fig. 4(n). They tend to reduce the space required for twin formation by both twin mechanisms (Fig. 7(a)–(b)). In $[1\bar{1}0]$ tension, however, SP formation is also profuse but the frequency of intersections and lock formation is lower. Consequently, in the early stages of straining, more twins develop

unconventionally for the [1$\bar{1}$0] orientation than the [111] orientation. With more [1$\bar{1}$0] tension, however, the SP intersections increase, causing some of the initially formed nanotwins to detwin.

Higher temperatures have similar effects as LD, in promoting SP nucleation and slowing down SP glide [95]. The result is a higher chance for twinning for the same SC orientation at 300 K than at 1 K. For the *A*-atom SC, this effect of temperature on twinning is more apparent than in the MEA SCs, since in the MEAs, some combination of LD and thermal vibrations exist at all temperatures.

In addition to LD, CSRO is shown to play an especially important role in dislocation nucleation. Calculations of strain distribution maps in Fig. 10 (as well as Figures S7-S8) show that higher degrees of CSRO in the form of larger CoCr clusters and Ni segregation correspond to larger regions of localized strains in the CoCr regions. Such an inhomogeneous distribution of strain calculated here has been observed experimentally in [46]. They reported that larger fluctuations in local strain in the CoCrNi MEA were associated with larger values of CSRO and that they appeared to be correlated with higher SFE, hardness, Young's modulus and yield strength. Consistent with their findings, we observe in simulation in Fig. 8, Fig. 11 and Fig. A.1, that the elastic modulus, SFE, and ultimate strength increase with increasing levels of CSRO. Here, we reveal that dislocations prefer to nucleate at the clusters that possess a combination of the lowest local unstable stacking fault energy (USFE) and highest shear strain concentrations. We identify that the strengthening with stronger CSRO partly arises from the increased difficulty in emitting dislocations from these sites when the USFE of the surrounding regions is higher. This finding implies that strengthening with CSRO can be expected when the USFE difference between the two neighboring segregated domains is large. Although the range of CSRO values, the strains they induce, and their physical properties, e.g., elastic modulus, strength and SFE, vary with processing and MPEA compositions, their influence on the dislocation nucleation found here ought to apply to other MPEAs with other compositions.

4. Conclusions

In this work, large-scale molecular dynamics (MD) simulations are performed to investigate the effects of lattice distortion (LD) and chemical short-range ordering (CSRO) on the tensile deformation of single crystal (SC) and nanocrystalline (NC) CoCrNi medium entropy alloys (MEAs). To quantify and elucidate their effects, calculations are repeated on a hypothetical *A*-atom material, which is a pure metal with no LD and CSRO but sharing virtually the same lattice constant and the same bulk elastic constants as CoCrNi. The main conclusions are:

- LD lowers the Young's modulus and strain for nucleation of Shockley partials (SPs).
- In all SC MEAs, the SPs nucleate inside the CoCr clusters, which generate the highest shear strains and have the lowest unstable stacking fault energy compared to those of the random MEA and Ni regions.
- Nanotwinning is more prevalent in the MEAs than the *A*-atom material, since larger LDs promote SP nucleation and both LDs and CSRO increase the resistance to SP propagation.
- The peak strengths of all NC MEAs are higher than that of the NC *A*-atom since after nucleation, and LDs and CSRO increase SP glide resistance.
- Introducing pre-existing nanotwins within the NC grains results in the highest strength and highest density of mobile SPs. Pre-existing twin boundaries (TBs) serve as strong barriers to non-planar SP glide, while also providing easy planes on which SPs can nucleate and glide.

Declaration of Competing Interest

The authors declare that they have no known competing financial interests or personal relationships that could have appeared to influence the work reported in this paper.

Acknowledgements

The authors would like to thank Dr. Wolfram G. Nöhring, Dr. Qing-Jie Li and Dr. Alexander Stukowski for helpful discussions. W.J. and I.J.B. would like to acknowledge funding from the Office of Naval Research under Grant No. N000141712810. The work of S.X. was supported in part by the Elings Prize Fellowship in Science offered by the California NanoSystems Institute on the UC Santa Barbara campus. S.X., Y.S., and I.J.B. gratefully acknowledges support from the Office of Naval Research under contract ONR BRC Grant N00014-18-1-2392. Use was made of computational facilities purchased with funds from the National Science Foundation (CNS-1725797) and administered by the Center for Scientific Computing (CSC). The CSC is supported by the CNSI and the Materials Research Science and Engineering Center (MRSEC; NSF DMR 1720256) at UC Santa Barbara. X.Y. would like to express his sincere gratitude for the financial support by National Science Foundation for Distinguished Young Scholars of China (11925203) and Natural Science Foundation of China (11672110).

Appendix A. Generalized stacking fault energy (GSFE) curves

We calculate the GSFE curves for the *A*-atom and various SC CoCrNi MEA samples (Fig. A.1(a)). With dimensions of $\sim$ 7.6 nm $\times$

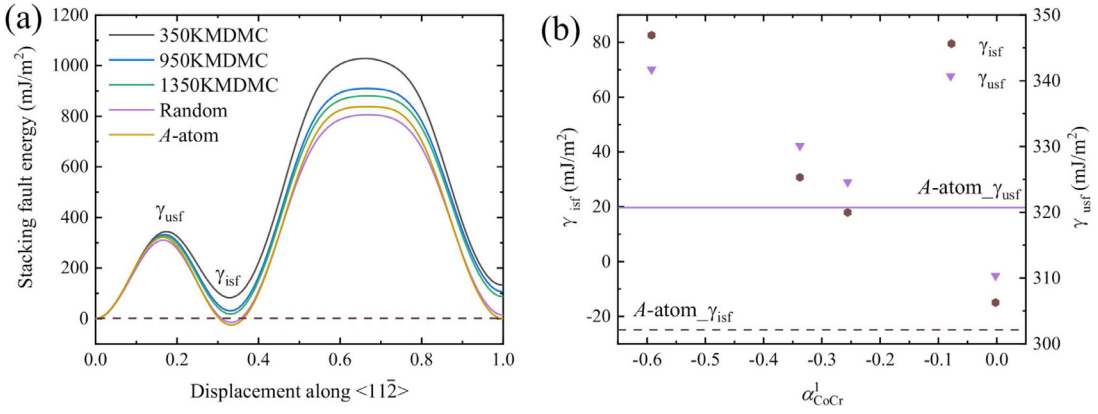

Fig. A.1. (a) GSFE curves for *A*-atom and various SC CoCrNi MEA samples. The unit length along the displacement direction is $a\sqrt{6}/2$, where a is the corresponding lattice constant for various samples. (b) The intrinsic SFE γ^{isf} and unstable SFE γ^{usf} as functions of α^1_{CoCr} for various SC CoCrNi MEA samples. In (b), γ^{isf} and γ^{usf} of *A*-atom sample are also shown as the dashed line and the solid line for comparison. Here, the definitions of random, 350KMDMC, 950KMDMC and 1350KMDMC follow Fig. 2.

Table B.1
Lattice parameter a, cohesive energy E_{coh}, elastic constants C_{11}, C_{12}, and C_{44}, intrinsic and unstable stacking fault energies γ_{isf} and γ_{usf} for random CoCrNi and *A*-atom samples. Random and *A*-atom represent the sample with completely random atomic distribution and a mean-field CoCrNi produced by an *A*-atom potential, respectively.

Sample	a (Å)	E_{coh} (eV)	B (GPa)	C_{11} (GPa)	C_{12} (GPa)	C_{44} (GPa)	γ_{isf} (mJ/m^2)	γ_{usf} (mJ/m^2)
Random	3.556	−4.322	202.9	252.6	178.7	95.1	−14.97	310.34
A-atom	3.553	−4.326	208.3	265.7	179.6	100.4	−25.26	321.34

13.1 nm × 24.7 nm along *x*-, *y*- and *z*-axes, total number of atoms in the computational configurations comes to 216,000 atoms. The $[1\bar{1}0]$, $[11\bar{2}]$ and [111] crystallographic directions lie parallel to the *x*-, *y*- and *z*-axes, respectively. PBCs are only applied in the *x* and *y* directions. To obtain the GSFE curves, the upper half of each sample is displaced along the *y*-axis on the (111) plane. To ensure a good statistical representation, each GSFE curve for the SC CoCrNi MEA samples in Fig. A.1(a) is obtained by averaging the results of 120 CoCrNi configurations. Fig. A.1(b) also includes the intrinsic SFE γ^{isf} and unstable SFE γ^{usf} for various SC CoCrNi MEA samples as functions of α^1_{CoCr}.

Appendix B. Characterization of the *A*-atom potential

To characterize the reliability of the *A*-atom potential, we further compare some basic properties of random CoCrNi and *A*-atom samples, such as lattice parameter, cohesive energy, and local maxima and minima in their generalized stacking fault energy landscapes. The results are shown in Table B.1. Overall, the values between random CoCrNi and *A*-atom samples are similar, demonstrating that the *A*-atom EAM potential is sufficiently reliable for mechanical calculations.

Appendix C. Estimation of the average velocity of SP motion in the *A*-atom and CoCrNi samples

To obtain an estimate for the average velocity of the Shockley partials (SPs), we consider the CoCrNi and *A*-atom SC samples deformed in tension in the $[1\bar{1}0]$ direction at 1 K. This choice aims to remove the effects of the GBs in the NC samples and minimize the effects of Lomer and Hirth locks that tend to form much more readily in the early stages of tension testing along [111] direction than the $[1\bar{1}0]$ direction. We begin with SF density-time and SP dislocation density-time curves, which follow the SF density-strain curves and SP density-strain curves shown in Fig. 4, since time is proportional to strain. Next by assuming that, in the early stages of straining, every SF forms from the glide of SPs, the area of SF is then be estimated by the product of the line length of SP dislocation and its gliding distance. Next, the SP displacement is obtained by dividing the SF density by the SP dislocation density. Fig. C.2 compares the resulting SP displacement-time curves for the *A*-atom and three CoCrNi SC samples. These plots begin at the time when the first SP dislocation has nucleated. In the early stages of plastic deformation, the curves are linear up to a certain strain level, marked by the vertical red line in each case. The aver-

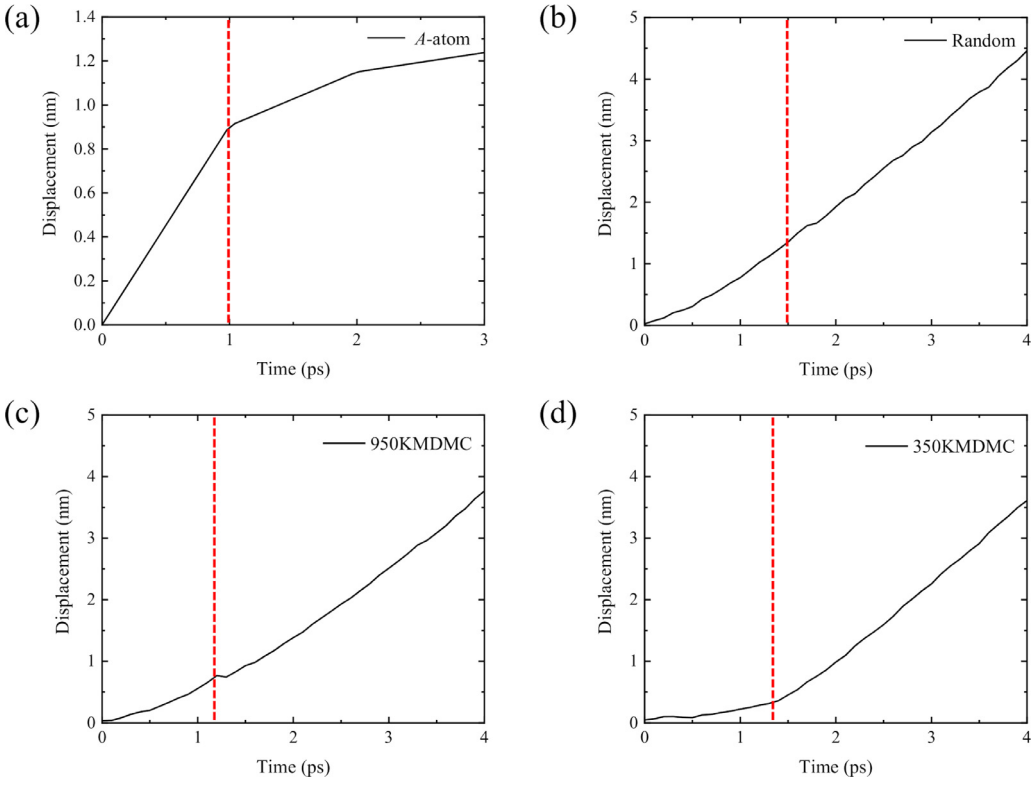

Fig. C.2. SP dislocation displacement-time curves for four SC samples deformed via tension along the $[1\bar{1}0]$ direction at 1 K: (a) *A*-atom, (b) random, (c) 950KMDMC and (d) 350KMDMC. Here the definitions of random, 350KMDMC and 950KMDMC follow Fig. 2. Only the early stage of each curve (marked by the vertical red line) is utilized to calculate the average SP speed.

age SP speed can be estimated by the derivative of SP displacement with respect to time in this region. Fig. 6 compares the average SP speed resulting from this calculation for the four SC [1$\bar{1}$0] samples.

Supplementary material

Supplementary material associated with this article can be found, in the online version, at 10.1016/j.actamat.2020.08.044

References

[1] Y. Zhang, T.T. Zuo, Z. Tang, M.C. Gao, K.A. Dahmen, P.K. Liaw, Z.P. Lu, Microstructures and properties of high-entropy alloys, Prog. Mater. Sci. 61 (2014) 1–93.
[2] Y. Ye, Q. Wang, J. Lu, C. Liu, Y. Yang, High-entropy alloy: challenges and prospects, Mater. Today 19 (6) (2016) 349–362.
[3] E. Pickering, N. Jones, High-entropy alloys: a critical assessment of their founding principles and future prospects, Int. Mater. Rev. 61 (3) (2016) 183–202.
[4] H. Diao, R. Feng, K.A. Dahmen, P. Liaw, Fundamental deformation behavior in high-entropy alloys: An overview, Curr. Opin. Solid State Mater. Sci. 21 (5) (2017) 252–266.
[5] D.B. Miracle, O.N. Senkov, A critical review of high entropy alloys and related concepts, Acta Mater. 122 (2017) 448–511.
[6] E. George, W. Curtin, C.C. Tasan, High entropy alloys: A focused review of mechanical properties and deformation mechanisms, Acta Mater. 188 (2019) 435–474.
[7] B. Cantor, Multicomponent and high entropy alloys, Entropy 16 (9) (2014) 4749–4768.
[8] Y. Jien-Wei, Recent progress in high entropy alloys, Ann. Chim. Sci. Mat 31 (6) (2006) 633–648.
[9] M.-H. Tsai, J.-W. Yeh, High-entropy alloys: a critical review, Mater. Res. Lett. 2 (3) (2014) 107–123.
[10] S.S. Sohn, A. Kwiatkowski da Silva, Y. Ikeda, F. Körmann, W. Lu, W.S. Choi, B. Gault, D. Ponge, J. Neugebauer, D. Raabe, Ultrastrong medium-entropy single-phase alloys designed via severe lattice distortion, Adv. Mater. 31 (8) (2019) 1807142.
[11] E. Ma, Unusual dislocation behavior in high-entropy alloys, Scr. Mater. 181 (2020) 127–133.
[12] W. Nöhring, W. Curtin, Design using randomness: a new dimension for metallurgy, Scr. Mater. 187 (2020) 210–215.
[13] Z. Li, S. Zhao, R.O. Ritchie, M.A. Meyers, Mechanical properties of high-entropy alloys with emphasis on face-centered cubic alloys, Prog. Mater. Sci. 102 (2019) 296–345.
[14] B. Cantor, I. Chang, P. Knight, A. Vincent, Microstructural development in equiatomic multicomponent alloys, Mater. Sci. Eng. A 375 (2004) 213–218.
[15] Z. Wu, H. Bei, F. Otto, G.M. Pharr, E.P. George, Recovery, recrystallization, grain growth and phase stability of a family of FCC-structured multi-component equiatomic solid solution alloys, Intermetallics 46 (2014) 131–140.
[16] B. Gludovatz, A. Hohenwarter, D. Catoor, E.H. Chang, E.P. George, R.O. Ritchie, A fracture-resistant high-entropy alloy for cryogenic applications, Science 345 (6201) (2014) 1153–1158.
[17] B. Gludovatz, A. Hohenwarter, K.V. Thurston, H. Bei, Z. Wu, E.P. George, R.O. Ritchie, Exceptional damage-tolerance of a medium-entropy alloy CrCoNi at cryogenic temperatures, Nat. Commun. 7 (1) (2016) 1–8.
[18] Z. Zhang, H. Sheng, Z. Wang, B. Gludovatz, Z. Zhang, E.P. George, Q. Yu, S.X. Mao, R.O. Ritchie, Dislocation mechanisms and 3D twin architectures generate exceptional strength-ductility-toughness combination in CrCoNi medium-entropy alloy, Nat. Commun. 8 (1) (2017) 1–8.
[19] G. Laplanche, A. Kostka, C. Reinhart, J. Hunfeld, G. Eggeler, E. George, Reasons for the superior mechanical properties of medium-entropy CrCoNi compared to high-entropy CrMnFeCoNi, Acta Mater. 128 (2017) 292–303.
[20] J. Miao, C. Slone, T. Smith, C. Niu, H. Bei, M. Ghazisaeidi, G. Pharr, M.J. Mills, The evolution of the deformation substructure in a Ni-Co-Cr equiatomic solid solution alloy, Acta Mater. 132 (2017) 35–48.
[21] Y. Zhao, T. Yang, Y. Tong, J. Wang, J. Luan, Z. Jiao, D. Chen, Y. Yang, A. Hu, C. Liu, et al., Heterogeneous precipitation behavior and stacking-fault-mediated deformation in a CoCrNi-based medium-entropy alloy, Acta Mater. 138 (2017) 72–82.
[22] C. Slone, S. Chakraborty, J. Miao, E.P. George, M.J. Mills, S. Niezgoda, Influence of deformation induced nanoscale twinning and FCC-HCP transformation on hardening and texture development in medium-entropy CrCoNi alloy, Acta Mater. 158 (2018) 38–52.
[23] B. Uzer, S. Picak, J. Liu, T. Jozaghi, D. Canadinc, I. Karaman, Y. Chumlyakov, I. Kireeva, On the mechanical response and microstructure evolution of NiCoCr single crystalline medium entropy alloys, Mater. Res. Lett. 6 (8) (2018) 442–449.
[24] W. Guo, Z. Pei, X. Sang, J.D. Poplawsky, S. Bruschi, J. Qu, D. Raabe, H. Bei, Shape-preserving machining produces gradient nanolaminate medium entropy alloys with high strain hardening capability, Acta Mater. 170 (2019) 176–186.
[25] Q. Ding, X. Fu, D. Chen, H. Bei, B. Gludovatz, J. Li, Z. Zhang, E.P. George, Q. Yu, T. Zhu, et al., Real-time nanoscale observation of deformation mechanisms in CrCoNi-based medium-to high-entropy alloys at cryogenic temperatures, Mater. Today 25 (2019) 21–27.
[26] M. Naeem, H. He, F. Zhang, H. Huang, S. Harjo, T. Kawasaki, B. Wang, S. Lan, Z. Wu, F. Wang, et al., Cooperative deformation in high-entropy alloys at ultralow temperatures, Sci. Adv. 6 (13) (2020) eaax4002.
[27] B. Schuh, B. Völker, J. Todt, K.S. Kormout, N. Schell, A. Hohenwarter, Influence of annealing on microstructure and mechanical properties of a nanocrystalline CrCoNi medium-entropy alloy, Materials 11 (5) (2018) 662.
[28] P. Sathiyamoorthi, J. Moon, J.W. Bae, P. Asghari-Rad, H.S. Kim, Superior cryogenic tensile properties of ultrafine-grained CoCrNi medium-entropy alloy produced by high-pressure torsion and annealing, Scr. Mater. 163 (2019) 152–156.
[29] B. Schuh, R. Pippan, A. Hohenwarter, Tailoring bimodal grain size structures in nanocrystalline compositionally complex alloys to improve ductility, Mater. Sci. Eng. A 748 (2019) 379–385.
[30] B. Gan, J.M. Wheeler, Z. Bi, L. Liu, J. Zhang, H. Fu, Superb cryogenic strength of equiatomic CrCoNi derived from gradient hierarchical microstructure, J. Mater. Sci. Technol. 35 (6) (2019) 957–961.
[31] G.D. Sathiaraj, W. Skrotzki, A. Pukenas, R. Schaarschuch, R.J. Immanuel, S. Panigrahi, J.A. Chelvane, S.S. Kumar, Effect of annealing on the microstructure and texture of cold rolled CrCoNi medium-entropy alloy, Intermetallics 101 (2018) 87–98.
[32] P. Sathiyamoorthi, P. Asghari-Rad, J.W. Bae, H.S. Kim, Fine tuning of tensile properties in CrCoNi medium entropy alloy through cold rolling and annealing, Intermetallics 113 (2019) 106578.
[33] L. Chai, K. Xiang, J. Xia, V. Fallah, K.L. Murty, Z. Yao, B. Gan, Effects of pulsed laser surface treatments on microstructural characteristics and hardness of CrCoNi medium-entropy alloy, Philos. Mag. 99 (24) (2019) 3015–3031.
[34] W. Guo, Z. Pei, X. Sang, J.D. Poplawsky, S. Bruschi, J. Qu, D. Raabe, H. Bei, Shape-preserving machining produces gradient nanolaminate medium entropy alloys with high strain hardening capability, Acta Mater. 170 (2019) 176–186.
[35] Y. Zhou, Y. Zhang, F. Wang, G. Chen, Phase transformation induced by lattice distortion in multiprincipal component $CoCrFeNiCu_xAl_{1-x}$ solid-solution alloys, Appl. Phys. Lett. 92 (24) (2008) 241917.
[36] H.S. Oh, D. Ma, G.P. Leyson, B. Grabowski, E.S. Park, F. Körmann, D. Raabe, Lattice distortions in the FeCoNiCrMn high entropy alloy studied by theory and experiment, Entropy 18 (9) (2016) 321.
[37] L. Owen, E. Pickering, H. Playford, H. Stone, M. Tucker, N. Jones, An assessment of the lattice strain in the CrMnFeCoNi high-entropy alloy, Acta Mater. 122 (2017) 11–18.
[38] Y. Zhao, T. Nieh, Correlation between lattice distortion and friction stress in Ni-based equiatomic alloys, Intermetallics 86 (2017) 45–50.
[39] Y. Zhao, Z. Lei, Z. Lu, J. Huang, T. Nieh, A simplified model connecting lattice distortion with friction stress of Nb-based equiatomic high-entropy alloys, Mater. Res. Lett. 7 (8) (2019) 340–346.
[40] P. Wang, Y. Wu, J. Liu, H. Wang, Impacts of atomic scale lattice distortion on dislocation activity in high-entropy alloys, Extreme Mech. Lett. 17 (2017) 38–42.
[41] B. Yin, W. Curtin, Origin of high strength in the CoCrFeNiPd high-entropy alloy, Mater. Res. Lett. 8 (6) (2020) 209–215.
[42] M. Laurent-Brocq, A. Akhatova, L. Perrière, S. Chebini, X. Sauvage, E. Leroy, Y. Champion, Insights into the phase diagram of the CrMnFeCoNi high entropy alloy, Acta Mater. 88 (2015) 355–365.
[43] J.M. Cowley, X-Ray measurement of order in single crystals of Cu_3Au, J. Appl. Phys. 21 (1) (1950) 24–30.
[44] J. Cowley, An approximate theory of order in alloys, Phys. Rev. 77 (5) (1950) 669.
[45] D. de Fontaine, The number of independent pair-correlation functions in multicomponent systems, J. Appl. Crystall. 4 (1) (1971) 15–19.
[46] R. Zhang, S. Zhao, J. Ding, Y. Chong, T. Jia, C. Ophus, M. Asta, R.O. Ritchie, A.M. Minor, Short-range order and its impact on the CrCoNi medium-entropy alloy, Nature 581 (7808) (2020) 283–287.
[47] A. Sharma, P. Singh, D.D. Johnson, P.K. Liaw, G. Balasubramanian, Atomistic clustering-ordering and high-strain deformation of an $Al_{0.1}$CrCoFeNi high-entropy alloy, Sci. Rep. 6 (2016) 31028.
[48] W.-M. Choi, Y.H. Jo, S.S. Sohn, S. Lee, B.-J. Lee, Understanding the physical metallurgy of the CoCrFeMnNi high-entropy alloy: an atomistic simulation study, npj Comput. Mater. 4 (2018) 1.
[49] J. Li, Q. Fang, B. Liu, Y. Liu, Transformation induced softening and plasticity in high entropy alloys, Acta Mater. 147 (2018) 35–41.
[50] Q. Fang, Y. Chen, J. Li, C. Jiang, B. Liu, Y. Liu, P.K. Liaw, Probing the phase transformation and dislocation evolution in dual-phase high-entropy alloys, Int. J. Plast. 114 (2019) 161–173.
[51] F. Yuan, W. Cheng, S. Zhang, X. Liu, X. Wu, Atomistic simulations of tensile deformation in a CrCoNi medium-entropy alloy with heterogeneous grain structures, Materialia 9 (2020) 100565.
[52] M. Bahramyan, R.T. Mousavian, D. Brabazon, Study of the plastic deformation mechanism of TRIP-TWIP high entropy alloys at the atomic level, Int. J. Plast. 127 (2020) 102649.
[53] J. Ding, Q. Yu, M. Asta, R.O. Ritchie, Tunable stacking fault energies by tailoring local chemical order in CrCoNi medium-entropy alloys, Proc. Natl. Acad. Sci. 115 (36) (2018) 8919–8924.
[54] S. Yin, J. Ding, M. Asta, R.O. Ritchie, Ab initio modeling of the energy landscape for screw dislocations in body-centered cubic high-entropy alloys, npj Comput. Mater. 6 (2020) 110.
[55] Q.-J. Li, H. Sheng, E. Ma, Strengthening in multi-principal element alloys with local-chemical-order roughened dislocation pathways, Nat. Commun. 10 (1) (2019) 1–11.

[56] E. Antillon, C. Woodward, S. Rao, B. Akdim, T. Parthasarathy, Chemical short range order strengthening in a model FCC high entropy alloy, Acta Mater. 190 (2020) 29–42.
[57] F. Zhang, S. Zhao, K. Jin, H. Xue, G. Velisa, H. Bei, R. Huang, J. Ko, D. Pagan, J. Neuefeind, et al., Local structure and short-range order in a NiCoCr solid solution alloy, Phys. Rev. Lett. 118 (20) (2017) 205501.
[58] Z. Wang, J. Li, Q. Fang, B. Liu, L. Zhang, Investigation into nanoscratching mechanical response of AlCrCuFeNi high-entropy alloys using atomic simulations, Appl. Surf. Sci. 416 (2017) 470–481.
[59] H.-S. Do, B.-J. Lee, Origin of radiation resistance in multi-principal element alloys, Sci. Rep. 8 (2018) 16015.
[60] C. Varvenne, A. Luque, W.G. Nöhring, W.A. Curtin, Average-atom interatomic potential for random alloys, Phys. Rev. B 93 (10) (2016) 104201.
[61] R.W. Smith, G.S. Was, Application of molecular dynamics to the study of hydrogen embrittlement in Ni-Cr-Fe alloys, Phys. Rev. B 40 (15) (1989) 10322.
[62] S. Xu, E. Hwang, W.-R. Jian, Y. Su, I.J. Beyerlein, Atomistic calculations of the generalized stacking fault energies in two refractory multi-principal element alloys, Intermetallics 124 (2020) 106844.
[63] S. Plimpton, Fast parallel algorithms for short-range molecular dynamics, J. Comp. Phys. 117 (1) (1995) 1–19.
[64] F.-H. Cao, Y.-J. Wang, L.-H. Dai, Novel atomic-scale mechanism of incipient plasticity in a chemically complex CrCoNi medium-entropy alloy associated with inhomogeneity in local chemical environment, Acta Mater. (2020).
[65] W. Brostow, J.-P. Dussault, B.L. Fox, Construction of voronoi polyhedra, J. Comput. Phys. 29 (1) (1978) 81–92.
[66] S.Z. Chavoshi, S. Xu, Tension-compression asymmetry in plasticity of nanotwinned 3C-SiC nanocrystals, J. Appl. Phys. 124 (9) (2018) 095103.
[67] S.Z. Chavoshi, S. Xu, Twinning effects in the single/nanocrystalline cubic silicon carbide subjected to nanoindentation loading, Materialia 3 (2018) 304–325.
[68] S. Xu, L. Xiong, Y. Chen, D.L. McDowell, Comparing EAM potentials to model slip transfer of sequential mixed character dislocations across two symmetric tilt grain boundaries in Ni, JOM 69 (5) (2017) 814–821.
[69] H. Suzuki, C. Barrett, Deformation twinning in silver-gold alloys, Acta Metall. 6 (3) (1958) 156–165.
[70] T. Blewitt, R. Coltman, J. Redman, Low-temperature deformation of copper single crystals, J. Appl. Phys. 28 (6) (1957) 651–660.
[71] Y. Zhu, X. Liao, S. Srinivasan, Y. Zhao, M. Baskes, F. Zhou, E. Lavernia, Nucleation and growth of deformation twins in nanocrystalline aluminum, Appl. Phys. Lett. 85 (21) (2004) 5049–5051.
[72] I. Karaman, H. Sehitoglu, K. Gall, Y.I. Chumlyakov, H. Maier, Deformation of single crystal Hadfield steel by twinning and slip, Acta Mater. 48 (6) (2000) 1345–1359.
[73] F. Cao, I.J. Beyerlein, F.L. Addessio, B.H. Sencer, C.P. Trujillo, E.K. Cerreta, G.T. Gray III, Orientation dependence of shock-induced twinning and substructures in a copper bicrystal, Acta Mater. 58 (2) (2010) 549–559.
[74] A. Stukowski, V.V. Bulatov, A. Arsenlis, Automated identification and indexing of dislocations in crystal interfaces, Modelling Simul. Mater. Sci. Eng. 20 (8) (2012) 085007.
[75] A. Stukowski, Visualization and analysis of atomistic simulation data with OVITO–the Open Visualization Tool, Modelling Simul. Mater. Sci. Eng. 18 (1) (2009) 015012.
[76] Z. Yan, Y. Lin, Lomer-Cottrell locks with multiple stair-rod dislocations in a nanostructured Al alloy processed by severe plastic deformation, Mater. Sci. Eng. A 747 (2019) 177–184.
[77] A. Stukowski, Computational analysis methods in atomistic modeling of crystals, JOM 66 (3) (2014) 399–407.
[78] D. Utt, A. Stukowski, K. Albe, Grain boundary structure and mobility in high--entropy alloys: A comparative molecular dynamics study on a Σ11 symmetrical tilt grain boundary in face-centered cubic CuNiCoFe, Acta Mater. 186 (2020) 11–19.
[79] W. Staubwasser, On work-hardening of aluminium-single crystals (99.99-percent Al) and its interpretation, Acta Metall. 7 (1) (1959) 43–50.
[80] Y. Kawasaki, T. Takeuchi, Cell structures in copper single crystals deformed in the [001] and [111] axes, Scripta Metall. 14 (2) (1980) 183–188.
[81] P. Franciosi, A. Zaoui, Multislip tests on copper crystals: a junctions hardening effect, Acta Metall. 30 (12) (1982) 2141–2151.
[82] N. Hansen, X. Huang, Microstructure and flow stress of polycrystals and single crystals, Acta Mater. 46 (5) (1998) 1827–1836.
[83] I. Karaman, H. Sehitoglu, Y.I. Chumlyakov, H.J. Maier, I. Kireeva, The effect of twinning and slip on the Bauschinger effect of Hadfield steel single crystals, Metall. Mater. Trans. A 32 (13) (2001) 695–706.
[84] J.R. Rice, Dislocation nucleation from a crack tip: an analysis based on the Peierls concept, J. Mech. Phys. Solids 40 (2) (1992) 239–271.
[85] S. Mahajan, Critique of mechanisms of formation of deformation, annealing and growth twins: Face-centered cubic metals and alloys, Scr. Mater. 68 (2) (2013) 95–99.
[86] J. Wang, H. Huang, Shockley partial dislocations to twin: another formation mechanism and generic driving force, Appl. Phys. Lett. 85 (24) (2004) 5983–5985.
[87] Y. Zhu, X. Liao, X. Wu, Deformation twinning in nanocrystalline materials, Prog. Mater. Sci. 57 (1) (2012) 1–62.
[88] I.J. Beyerlein, X. Zhang, A. Misra, Growth twins and deformation twins in metals, Annu. Rev. Mater. Res. 44 (2014) 329–363.
[89] F. Shimizu, S. Ogata, J. Li, Theory of shear banding in metallic glasses and molecular dynamics calculations, Mater. Trans. (2007) 0710160231.
[90] M. Hasan, Y. Liu, X. An, J. Gu, M. Song, Y. Cao, Y. Li, Y. Zhu, X. Liao, Simultaneously enhancing strength and ductility of a high-entropy alloy via gradient hierarchical microstructures, Int. J. Plast. 123 (2019) 178–195.
[91] X. Xu, P. Liu, Z. Tang, A. Hirata, S. Song, T. Nieh, P. Liaw, C. Liu, M. Chen, Transmission electron microscopy characterization of dislocation structure in a face-centered cubic high-entropy alloy $Al_{0.1}$CoCrFeNi, Acta Mater. 144 (2018) 107–115.
[92] B. Schuh, F. Mendez-Martin, B. Völker, E.P. George, H. Clemens, R. Pippan, A. Hohenwarter, Mechanical properties, microstructure and thermal stability of a nanocrystalline CoCrFeMnNi high-entropy alloy after severe plastic deformation, Acta Mater. 96 (2015) 258–268.
[93] X. Feng, J. Zhang, Z. Xia, W. Fu, K. Wu, G. Liu, J. Sun, Stable nanocrystalline NbMoTaW high entropy alloy thin films with excellent mechanical and electrical properties, Mater. Lett. 210 (2018) 84–87.
[94] K.-Y. Tsai, M.-H. Tsai, J.-W. Yeh, Sluggish diffusion in Co-Cr-Fe-Mn-Ni high-entropy alloys, Acta Mater. 61 (13) (2013) 4887–4897.
[95] D.L. Olmsted, L.G. Hector Jr, W. Curtin, R. Clifton, Atomistic simulations of dislocation mobility in Al, Ni and Al/Mg alloys, Modelling Simul. Mater. Sci. Eng. 13 (3) (2005) 371.